



2

**Carderock Division  
Naval Surface Warfare Center**

Bethesda, MD 20084-5000

**CARDEROCKDIV-92/002** September 1992

Ship Structures and Protection Department  
Research and Development Report

**A Coupled Finite Element - Boundary Element  
Method for Calculations of the Interaction  
Between an Explosion Bubble and a  
Submerged Compliant Target**

by

Charles D. Milligan  
Stephen Ziliacus

**DTIC**  
ELECTRIC  
NOV 30 1992  
**S B D**



92-30267  
SIP

Approved for public release; distribution is unlimited.

**THIS PAGE INTENTIONALLY LEFT BLANK**

UNCLASSIFIED

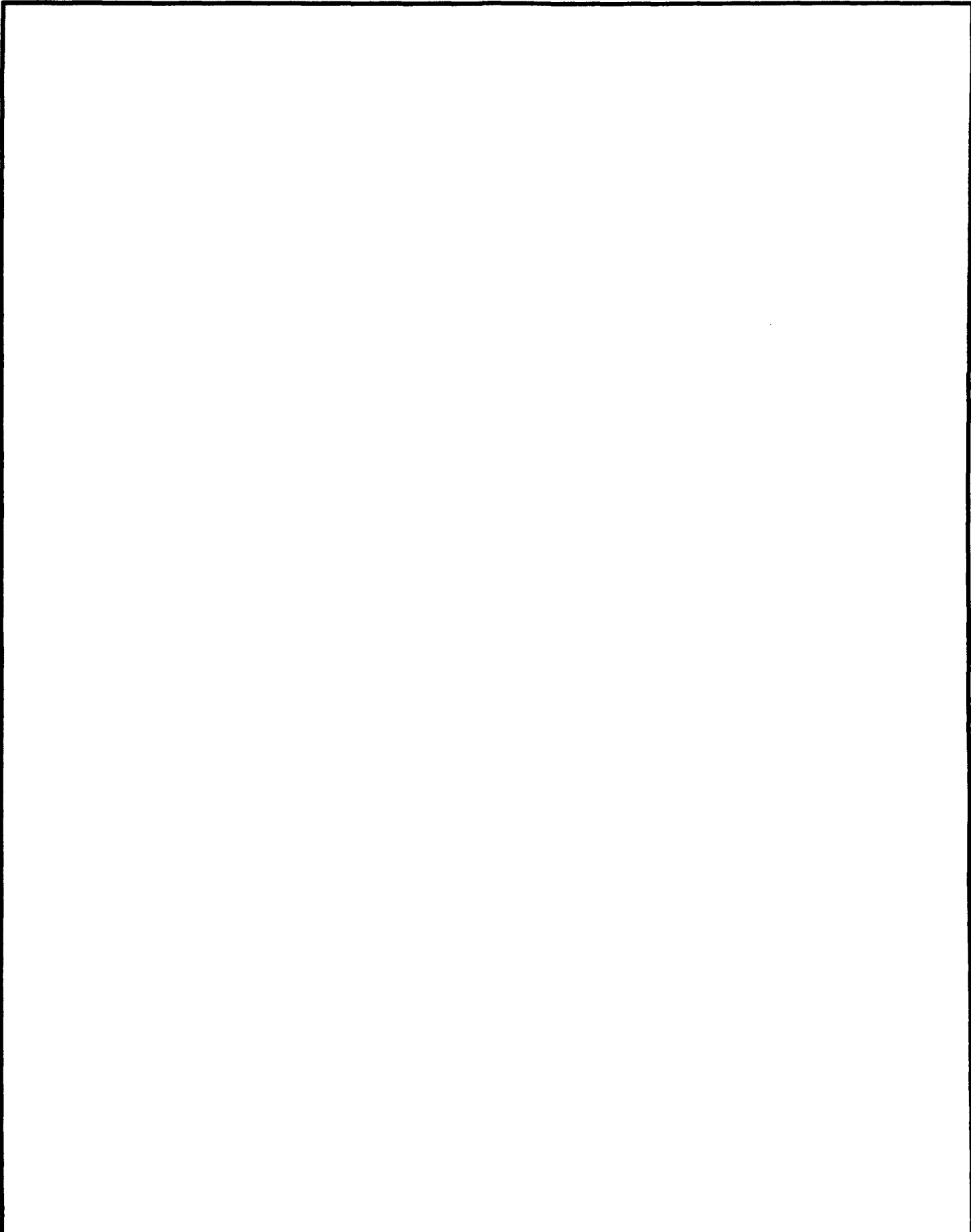
SECURITY CLASSIFICATION OF THIS PAGE

## REPORT DOCUMENTATION PAGE

|   |       |  |   |  |  |                             |
|---|-------|--|---|--|--|-----------------------------|
| 1a. REPORT SECURITY CLASSIFICATION<br><b>UNCLASSIFIED</b>   |       |  | 1b. RESTRICTIVE MARKINGS  |  |  |                             |
| 2a. SECURITY CLASSIFICATION AUTHORITY   |       |  | 3. DISTRIBUTION/AVAILABILITY OF REPORT  |  |  |                             |
| 2b. DECLASSIFICATION/DOWNGRADING SCHEDULE   |       |  | Approved for public release; distribution is unlimited.                           |  |  |                             |
| 4. PERFORMING ORGANIZATION REPORT NUMBER(S)<br><b>CARDEROCKDIV-92/002</b>   |       |  | 5. MONITORING ORGANIZATION REPORT NUMBER(S)                                       |  |  |                             |
| 6a. NAME OF PERFORMING ORGANIZATION<br><b>Carderock Division<br/>Naval Surface Warfare Center</b>   |       | 6b. OFFICE SYMBOL<br>(If applicable)<br><b>Code 1750</b> |   | 7a. NAME OF MONITORING ORGANIZATION<br><b>David Taylor Model Basin<br/>Independent Research (IR) Program</b> |  |                             |
| 6c. ADDRESS (City, State, and ZIP Code)<br><b>Bethesda, MD 20084-5000</b>   |       |  | 7b. ADDRESS (City, State, and ZIP Code)<br><b>Bethesda, MD 20084-5000</b>         |  |  |                             |
| 8a. NAME OF FUNDING/SPONSORING ORGANIZATION<br><b>Independent Research</b>  |       | 8b. OFFICE SYMBOL<br>(If applicable)                     |   | 9. PROCUREMENT INSTRUMENT IDENTIFICATION NUMBER  |  |                             |
| 8c. ADDRESS (City, State, and ZIP Code)   |       |  | 10. SOURCE OF FUNDING NUMBERS   |  |  |                             |
|   |       |  | PROGRAM ELEMENT NO.   | PROJECT NO.  | TASK NO.                                 | WORK UNIT ACCESSION NO.     |
| 11. TITLE (Include Security Classification)<br><b>A Coupled Finite Element - Boundary Element Method for Calculations of the Interaction Between an Explosion Bubble and a Submerged Compliant Target</b>   |       |  |   |  |  |                             |
| 12. PERSONAL AUTHOR(S)<br><b>Milligan, Charles D., and Zilliagus, Stephen</b>   |       |  |   |  |  |                             |
| 13a. TYPE OF REPORT<br><b>Final</b>   |       | 13b. TIME COVERED<br>FROM <b>901001</b> TO <b>911001</b> |   | 14. DATE OF REPORT (YEAR, MONTH, DAY)<br><b>1992 September</b>   |  | 15. PAGE COUNT<br><b>52</b> |
| 16. SUPPLEMENTARY NOTATION  |       |  |   |  |  |                             |
| 17. COSATI CODES  |       |  | 18. SUBJECT TERMS (Continue on reverse if necessary and identify by block number) |  |  |                             |
| FIELD   | GROUP | SUB-GROUP  | Fluid-Structure Interaction   | Boundary Element   | Fluid Loading                            |                             |
|   |       |  | Bubble Collapse   | Numerical Prediction Method  | Whipping                                 |                             |
|   |       |  | Finite Element  | Cavitation   |  |                             |
| 19. ABSTRACT (Continue on reverse if necessary and identify by block number)<br><br>An axisymmetric boundary element flow algorithm is coupled with a finite element structural analyzer to perform interactive calculations of the growth and subsequent collapse of an explosion bubble near a submerged compliant structure. The validity of the program is established through direct comparisons with published experimental data. A parametric study of the interaction between a growing and collapsing bubble and a spherical shell is presented. The results show that if the stiffness of the shell is sufficiently low, then the mass of the shell is a critical parameter in the collapse problem. If the mass of the structure is high, a reentrant jet forms and is then directed towards the shell. As the mass of the spherical shell is decreased, the collapse becomes spherical with no jet formation. At the lowest structural mass for which calculations are performed, a jet directed away from the structure begins to form. The ratio of the depth of submergence to bubble maximum radius was also found to be a critical parameter in the collapse problem. When this ratio is large (greater than 100), the collapse is driven by interaction forces. However, for shallow submergence, buoyancy effects become more important than interaction forces. |       |  |   |  |  |                             |
| 20. DISTRIBUTION/AVAILABILITY OF ABSTRACT<br><input type="checkbox"/> UNCLASSIFIED/UNLIMITED <input checked="" type="checkbox"/> SAME AS RPT <input type="checkbox"/> DTIC USERS  |       |  |   | 21. ABSTRACT SECURITY CLASSIFICATION<br><b>UNCLASSIFIED</b>  |  |                             |
| 22a. NAME OF RESPONSIBLE INDIVIDUAL<br><b>Charles D. Milligan</b>   |       |  | 22b. TELEPHONE (Include Area Code)<br><b>(301) 227-4153</b>                       |  | 22c. OFFICE SYMBOL<br><b>Code 1750.1</b> |                             |

UNCLASSIFIED

SECURITY CLASSIFICATION OF THIS PAGE



SECURITY CLASSIFICATION OF THIS PAGE

UNCLASSIFIED

## CONTENTS

|  | Page |
|--|------|
| <b>Abstract</b> .....                            | 1    |
| <b>Administrative</b> .....                      | 1    |
| <b>Introduction</b> .....                        | 1    |
| Background .....                                 | 1    |
| Prior Work .....                                 | 2    |
| Organization of Study .....                      | 4    |
| <b>Theoretical Model</b> .....                   | 4    |
| Mathematical Formulation .....                   | 4    |
| Numerical Implementation .....                   | 9    |
| <b>Program Verification</b> .....                | 11   |
| Model Descriptions .....                         | 11   |
| Comparison of Results .....                      | 14   |
| <b>Comparison with Experimental Data</b> .....   | 15   |
| Description of Experiment .....                  | 15   |
| Numerical Solution .....                         | 16   |
| Comparison of Results .....                      | 18   |
| <b>Interaction with a Compliant Sphere</b> ..... | 19   |
| Model Description .....                          | 19   |
| Results .....                                    | 21   |
| Summary .....                                    | 24   |
| <b>Conclusion</b> .....                          | 24   |
| <b>References</b> .....                          | 43   |

## FIGURES

|   |    |
|---|----|
| 1. Schematic showing the coordinate system and the initial position of the bubble and the compliant spherical shell ..... | 26 |
| 2. Axisymmetric continuum element .....   | 27 |
| 3. Nodes and panels on the surface of the bubble and on the fluid-structure interface .....                               | 28 |
| 4. Schematic showing spring backed membrane and initial configuration of the vapor bubble .....                           | 29 |
| 5. Finite element idealization of spring backed membrane .....  | 29 |
| 6. Dimensionless normal velocity of membrane at $r = 0.0$ for $M^* = K^* = 2.0$ .....                                     | 30 |

**FIGURES (Continued)**

|   | Page |
|---|------|
| 7. Dimensionless pressure $P_m/\Delta P$ on membrane at $r = 0.0$ versus separation on north and south poles of the bubble $(z_{np}-z_{sp})/R_{max}$ for $M^* = K^* = 2.0$ .....  | 30   |
| 8. Schematic showing experimental set-up for compliant coating experiments of Shima, Tomita, Gibson, and Blake .....  | 31   |
| 9. Finite element idealization of compliant coating .....   | 31   |
| 10. Comparison of results of present calculations and data from experiments of Shima, Tomita, Gibson, and Blake. Plot of $z_c/R_{max}$ versus $M^*$ for $Z_o = 1.14 R_{max}$ .....  | 32   |
| 11. Comparison of results of present calculations and data from experiments of Shima, Tomita, Gibson, and Blake. Plot of $z_c/R_{max}$ versus $M^*$ for $Z_o = 1.43 R_{max}$ .....  | 32   |
| 12. Comparison of results of present calculations and data from experiments of Shima, Tomita, Gibson, and Blake. Plot of $z_c/R_{max}$ versus $M^*$ for $Z_o = 1.71 R_{max}$ .....  | 33   |
| 13. Schematic showing coordinate system, spherical shell, and initial position of the explosion bubble .....  | 34   |
| 14. Finite element idealization of spherical shell .....  | 34   |
| 15. Height of north and south poles of the bubble versus time .....   | 35   |
| 16. Bubble collapse profiles at various times for collapse near rigid shell and compliant shells of $M^* = 226, 76,$ and $56$ .....   | 36   |
| 17. Velocity (positive outward into fluid) of the north pole of the shell versus time .....   | 38   |
| 18. Velocity (positive outward into fluid) of the south pole of the shell versus time .....   | 38   |
| 19. Displacement of the north pole of the sphere versus time .....  | 39   |
| 20. Effect of gravity on the motion of the north and south poles of the bubble. Plot of height of north and south poles of the bubble versus time for shells of $M^* = 226$ , at depths, $d = 206 R_{max}, 100 R_{max}, 10 R_{max}$ , ..... | 39   |
| 21. Bubble collapse profiles at various times near shell of $M^* = 226$ , at depths, $d = 206 R_{max}, 100 R_{max}, 10 R_{max}$ , .....   | 40   |

## ABSTRACT

*An axisymmetric boundary element flow algorithm is coupled with a finite element structural analyzer to perform interactive calculations of the growth and subsequent collapse of an explosion bubble near a submerged compliant structure. The validity of the program is established through direct comparisons with published experimental data. A parametric study of the interaction between a growing and collapsing bubble and a spherical shell is presented. The results show that if the stiffness of the shell is sufficiently low, the mass of the shell is a critical parameter in the collapse problem. If the mass of the structure is high, a reentrant jet forms and is directed towards the shell. As the mass of the spherical shell is decreased, the collapse becomes spherical with no jet formation. At the lowest structural mass for which calculations are performed, a jet directed away from the structure begins to form. The ratio of the depth of submergence to bubble maximum radius was also found to be a critical parameter in the collapse problem. When this ratio is large (greater than 100), the collapse is driven by interaction forces. However, for shallow submergence, buoyancy effects become more important than interaction forces.*

## ADMINISTRATIVE INFORMATION

This work was funded by the David Taylor Research Center Independent Research (IR) program under Work Unit 1750-161 for fiscal year 1991.

## INTRODUCTION

### BACKGROUND

The interaction between a growing and collapsing bubble and a submerged compliant structure is relevant to a number of engineering problems. Important examples include cavitation bubbles in fluid machinery and pulsating, collapsing underwater explosion bubbles near naval vessels. Experimental and theoretical studies have shown cavitation bubble collapse

DTIC QUALITY INSPECTED 2

1

|                    |                                     |
|--------------------|-------------------------------------|
| on For             |                                     |
| RA&I               | <input checked="" type="checkbox"/> |
| B                  | <input type="checkbox"/>            |
| Announced          | <input type="checkbox"/>            |
| Justification      |                                     |
| By                 |                                     |
| Distribution/      |                                     |
| Availability Codes |                                     |
| Dist               | Avail and/or<br>Special             |
| A-1                |                                     |

to be characterized by extremely high local velocity and overpressure, and high-speed liquid jet formation (Roberson and Crowe<sup>1</sup>). Recent studies have shown bubble centroid motion as well as jet strength and direction to be greatly influenced by the presence and nature of any nearby boundaries. The jet is known to cause surface erosion and pitting in turbomachinery. Ship propellers and other propulsion devices are especially susceptible to this type of damage (Arndt<sup>2</sup>). Collapsing cavitation bubbles are also responsible for structural vibration, noise and degradation of operating efficiency.

The detonation of a submerged explosive is characterized by the conversion of the original explosive material into a gas sphere at extremely high temperature and pressure. The inertia of the water surrounding the bubble and the compressible explosion products form a damped oscillatory system (Cole<sup>3</sup>). This oscillating bubble and entrained fluid can induce low frequency beam-like flexural motions in a nearby ship or submarine (Hicks<sup>4,5</sup>). This whipping phenomenon can lethally damage both ship structure and onboard equipment. As was the case for the cavitation bubble, the explosion bubble is greatly affected by the presence of any nearby boundaries. Under certain conditions, explosion bubble collapse is also accompanied by the formation of a high speed reentrant jet (Snay<sup>6</sup>). Here again, the jet strength and direction depend upon the proximity and compliance of any nearby boundaries. Studies on the damaging potential of underwater explosions have often focused on the initial shock wave emitted by the explosion. However, many investigations have shown that bubble collapse damage can be more extensive than shockwave damage.

## PRIOR WORK

To study the fundamental aspects of these problems, a number of theoretical, numerical, and experimental investigations have been conducted to examine the growth and collapse of vapor bubbles near plane boundaries. Collapse near a rigid wall is often characterized by the formation of a reentrant jet directed toward the wall (Benjamin and Ellis<sup>7</sup>). When the plane boundary is a free surface, a reentrant jet is also formed, but in this case, the jet is directed away from the boundary (Blake and Gibson<sup>8</sup>).

This complex interaction between the collapsing bubble and nearby boundaries has led a number of investigators to suggest application of a relatively flexible surface coating in order to redirect the reentrant jet and hence reduce bubble damage. Shima, Tomita, Gibson, and Blake<sup>9</sup> photographed the growth and collapse of spark generated vapor bubbles near planar surfaces covered with elastomeric coatings. Their study indicated that for some coating properties the jet was indeed redirected away from the solid boundary. Through this same study, detailed histories of the motion and shape of the bubbles are provided. Numerical simulations of the interaction between a growing and collapsing vapor bubble and a planar compliant surface have been conducted by Duncan and Zhang<sup>10,11</sup>. In these simulations, a boundary-integral flow algorithm was coupled to a finite difference representation of a spring-backed membrane. By equating pressure and velocity conditions in the flow and on the structure at the fluid-structure interface, Duncan and Zhang achieved a completely interactive simulation. The results of these simulations were in qualitative agreement with the experimental work of Shima, Tomita, Gibson and Blake<sup>9</sup>.

In the present study Duncan and Zhang's numerical method is extended to include an axisymmetric finite element structural idealization. The finite element model uses isoparametric continuum elements and a linear-elastic material model. This structural model allows one to include more detailed information about the structure and more complex structural geometries than the idealized, planar, spring-backed membrane used by Duncan and Zhang. As in Duncan and Zhang's model, inviscid, incompressible, potential flow is assumed and the boundary integral method is again employed to effect a solution of the potential flow problem. By matching the pressure and motion conditions at the fluid-structure interface, an interactive simulation is again achieved. In addition, the present work includes a polytropic model of the gas inside the bubble and a gravitational field, significant parameters that were not present in the work of Duncan and Zhang. These extensions make possible simulations of the growth and collapse of underwater explosion bubbles near target structures.

## ORGANIZATION OF STUDY

The following section contains an account of the theory behind the boundary integral formulation for the potential flow problem, a description of the finite element algorithm used to compute the structural response, and details of the numerical implementation for the bubble growth and collapse problem. Verification calculations are then given of the collapse of a bubble near a finite element idealization of a spring backed membrane. The results of these calculations are compared with the results of Duncan and Zhang. Next, an attempt is made to numerically simulate the experiments of Shima, Tomita, Gibson and Blake<sup>9</sup>. A parametric study of the growth and collapse of an explosion bubble near a compliant sphere is then presented. Finally, the results of the present work and suggested directions for future research are summarized.

## THEORETICAL MODEL

### MATHEMATICAL FORMULATION

A schematic showing the initial configuration of the bubble and a spherical structure is given in Fig. 1. A cylindrical coordinate system is used in the solution of the interaction problem. The radial coordinate is  $r$  and the circumferential angle is  $\theta$ . The problem is axisymmetric about the  $z$ -axis. The spherical structure has outer radius  $R_s$  and is centered at  $r = 0$ ,  $z = -R_s$ . The bubble is initially ( $t = 0$ ) spherical with radius  $R_0$ , and its center is located at  $z = Z_0$ . The pressure in the fluid far from the bubble,  $P_\infty$ , is maintained constant during the calculation. The theoretical model for the fluid is the one used by Duncan and Zhang. For clarity, parts of the presentations of Duncan and Zhang are included here in modified form.

The fluid motion is assumed to be incompressible and inviscid and therefore satisfies Laplace's equation:

$$\nabla^2 \phi = 0 \tag{1}$$

where  $\nabla^2$  is the Laplacian operator and  $\phi$  is the Eulerian velocity potential. The fluid velocity is equal to the gradient of the velocity potential,  $\vec{u} = \nabla\phi$ . On the surface of the bubble, the pressure in the fluid is equal to the pressure in the bubble,  $P_g$ . The condition imposed on  $\phi$  by this dynamic boundary condition can be written as Bernoulli's equation in material derivative form:

$$\frac{D\phi}{Dt} = \frac{1}{2}|\nabla\phi|^2 + \frac{P_\infty - P_g}{\rho} + g(z - Z_0) \quad (2)$$

where  $D/Dt$  is the derivative with respect to time following a fluid particle,  $\rho$  is the fluid density, and  $g$  is the acceleration due to gravity.

The noncondensable gases inside the bubble are assumed to have a polytropic behavior,

$$P_g V^\gamma = \text{const} \quad (3)$$

where  $\gamma$  is the polytropic constant and  $V$  is the volume of the bubble. The kinematic boundary condition on the surface of the bubble states that material points remain on the surface of the bubble:

$$\frac{D\vec{x}_c}{Dt} = \nabla\phi \quad (4)$$

where  $\vec{x}_c$  is the position vector to these material points.

For  $t < 0$ , the structure is motionless and statically loaded by uniform pressure,  $P_\infty$ , applied by the fluid. The response of the structure to the fluid loading is computed using a linear elastic finite element model. The structure is represented by an assemblage of discrete elements, interconnected at nodal points on the element boundaries. Each quadrilateral element has four nodes defined in orthogonal two dimensional coordinate space. There are two displacement degrees of freedom (dofs) associated with each nodal point. An axisymmetric element formulation is used such that each element represents the portion of the structure that is swept out by rotating the planar element one radian about the z-axis (see Fig. 2). The solution of a system of dynamic equations of motion provides the displacement, velocity, and acceleration of each nodal point in the element assemblage at discrete times. The system

equilibrium equations of the element assemblage are derived from virtual work considerations and are of the form:

$$M\ddot{\xi} + K\xi = R \quad (5)$$

where  $M$  is the global consistent mass matrix,

$K$  is the global stiffness matrix,

$R$  is consistent nodal load vector obtained from the total pressure in the fluid acting on the structure,

$\ddot{\xi}$  is the nodal acceleration vector (two components per node),

$\xi$  is the nodal displacement vector.

The consistent mass matrix contains structural mass information and provides the relationship between force at degree of freedom  $i$  and acceleration at dof  $j$ . The global stiffness matrix relates the applied force at dof  $i$  to resulting displacement at dof  $j$ . The  $K$  matrix is developed from material elastic stress-strain relations and linearized strain-displacement relations.

During the collapse, the fluid and the structure are coupled using linearized equations for the pressure and velocity in the two systems. These equations are satisfied at the undisturbed position of the fluid-structure interface:

$$\frac{\partial \xi_n}{\partial t} = -\frac{\partial \phi}{\partial n} \quad (6)$$

$$P_s(\vec{x}_s, t) = -\rho \frac{\partial \phi}{\partial t} + P_\infty \quad (7)$$

where  $\xi_n$  is the component of the surface displacement in the direction normal to the undisturbed surface of the structure,

$\partial \xi_n / \partial t$  is the normal velocity of the structure (positive outward into the fluid), and

$\partial \phi / \partial n$  is the derivative of the velocity potential in the direction normal to the undisturbed surface of the structure.

The second equation is the linearized Bernoulli equation and  $P_s(\vec{x}_s, t)$  is the fluid pressure applied to the structure at  $\vec{x}_s$ .

To show how the system of equations can be advanced in time, assume that at time  $t_i$  all dependent variables are known. The boundary conditions on the surface of the bubble, Eqs. 2 and 4, are integrated numerically to get the position of the surface of the bubble and the value of  $\phi$  on the bubble at time  $t_{i+1}$ . The finite element method is used to obtain the value of  $\partial\xi_n/\partial t = -\partial\phi/\partial n$  on the surface of the sphere at  $t_{i+1}$ . In order to move on to the next time step,  $t_{i+2}$ , the values of  $\nabla\phi$  must be known on the bubble surface for use in Eqs. 2 and 4. However, at this point only the value of  $\partial\phi/\partial s$  can be computed (where  $s$  is a coordinate along the bubble surface). Also, in order to find the value of  $\partial\phi/\partial n$  on the surface of the structure at  $t_{i+2}$ , the pressure must be known on the surface of the structure at  $t_{i+1}$  for use in the finite element calculation of the structural response. The pressure at  $t_{i+1}$  can be obtained from Bernoulli's equation (Eq. 7) if  $\partial\phi/\partial t$  is known. Thus, the value of  $\phi$  on the fluid-structure interface at time  $t_{i+1}$  must be found to obtain a finite difference approximation for  $\partial\phi/\partial t$ . To complete the problem, the values of  $\partial\phi/\partial n$  on the bubble surface and  $\phi$  on the surface of the structure are obtained by solving Laplace's equation in the form of an integral equation (Lamb<sup>12</sup>):

$$\int_{S_b+S_s} g(\vec{p}, \vec{q}) \frac{\partial\phi}{\partial n} dS_q - \int_{S_b+S_s} \frac{\partial g(\vec{p}, \vec{q})}{\partial n} \phi(\vec{q}) dS_q = 2\pi\phi(\vec{p}) \quad (8)$$

where  $S_b$  is the surface of the bubble,

$S_s$  is the interface between the structure and the fluid,

$\vec{p}$  is a field point that is on the surface  $S = S_b + S_s$ ,

$\vec{q}$  is the source point that is also on  $S$ ,  $g(\vec{p}, \vec{q}) = 1/|\vec{p} - \vec{q}|$ ,

$n$  is the normal to  $S$  directed outward from the fluid, and

$dS_q$  is the area element of  $S$  varying the point  $\vec{q}$ .

Since the problem is axisymmetric, the positions of the field points need only be considered in a single plane,  $\theta = 0$ . Once this equation is solved, the calculation can proceed on to the next time step or, with a companion form of this integral equation, the velocity and pressure can be found at any point in the fluid.

A special treatment is needed to start the calculation because the pressure distribution on the structure at  $t = 0$  is unknown. The following procedure

was used. From the linearized form of Bernoulli's equation (Eq. 7) evaluated on the structure at  $t = 0$ , it can be seen that the pressure on the structure is equal to the partial derivative of the velocity potential with respect to time evaluated on the surface of the structure. The calculation of the initial value of  $\partial\phi/\partial t$  on the structure is divided into two steps. In the first step, the initial value of  $\partial\phi/\partial n$  on the bubble surface is obtained from the integral equation (Eq. 8) with the initial value of  $\phi$  on the bubble obtained from an integrated form of the Rayleigh-Plesset equation for the case of a spherical bubble growing in an infinite fluid (see Batchelor<sup>13</sup>),

$$\phi_0 = -\frac{2R_0}{3\rho} \left( \frac{P_{g0}}{(1-\gamma)} (1 - \alpha^{3\gamma-3}) - P_\infty (1 - \alpha^{-3}) \right) \quad (9)$$

where  $P_{g0}$  is the pressure inside the bubble at the start of the calculation and  $\alpha = R_0/R_{max}$ . Since the structure is initially motionless, the value of  $\partial\phi/\partial n$  on the structure is given by

$$\frac{\partial\phi}{\partial n} = \frac{\partial\xi_n}{\partial t} = 0. \quad (10)$$

The values of  $\partial\phi/\partial t$  on the bubble are then obtained using Bernoulli's equation in the form

$$\frac{\partial\phi}{\partial t} = -\frac{1}{2} \left( \frac{\partial\phi}{\partial n} \right)^2 + \frac{P_\infty - P_g}{\rho} \quad (11)$$

where the fact that  $\partial\phi/\partial s = 0$  at  $t = 0$  ( $s$  is the direction along the bubble surface) has been used. In the second step of the calculation, it is noted that the partial derivative of  $\phi$  with respect to time also satisfies Laplace's equation:

$$\nabla^2 \left( \frac{\partial\phi}{\partial t} \right) = 0. \quad (12)$$

Thus, the integral equation (Eq. 8) is valid with  $\phi$  replaced by  $\partial\phi/\partial t$ . On the bubble,  $\partial\phi/\partial t$  is obtained from the first step described above. On the surface of the structure,

$$\rho \frac{\partial\phi}{\partial t} = m \frac{\partial}{\partial n} \frac{\partial\phi}{\partial t}. \quad (13)$$

The value of  $\partial\phi/\partial t$  on the structure and thus, the pressure on the structure at  $t = 0$  can be obtained by solving the integral equation for  $\partial\phi/\partial t$ .

## NUMERICAL IMPLEMENTATION

In the numerical model, the surface of the bubble is approximated by a set of panels each of which is obtained by rotating a straight line in the  $\theta = 0$  plane about the  $z$ -axis (see Fig. 3). The bubble is composed of  $n_b$  of these panels. The interface between the fluid and the structure is modeled by a set of  $n_s$  equal length panels. Field points (nodes) are taken at the positions where the line of intersection of two adjacent panels pierces the  $\theta = 0$  plane. A predictor-corrector scheme sometimes referred to as Heun's method (see Ferziger<sup>14</sup>) is used to perform the temporal integration of the boundary conditions on the bubble. The  $r$  and  $z$  coordinates of the nodes on the bubble and the corresponding values of  $\phi$  at  $t_{i+1}$  are expressed in vector form as:

Predictor step:

$$\begin{Bmatrix} \bar{r}_{i+1}^j \\ \bar{z}_{i+1}^j \\ \bar{\phi}_{i+1}^j \end{Bmatrix} = \begin{Bmatrix} r_i^j \\ z_i^j \\ \phi_i^j \end{Bmatrix} + (t_{i+1} - t_i) \begin{Bmatrix} u_i^j \\ w_i^j \\ \frac{1}{2}|\nabla\phi_i^j|^2 + \frac{P_\infty - P_g}{\rho} \end{Bmatrix} \quad (14)$$

Corrector step:

$$\begin{Bmatrix} r_{i+1}^j \\ z_{i+1}^j \\ \phi_{i+1}^j \end{Bmatrix} = \begin{Bmatrix} r_i^j \\ z_i^j \\ \phi_i^j \end{Bmatrix} + \frac{(t_{i+1} - t_i)}{2} \begin{Bmatrix} u_i^j + \bar{u}_{i+1}^j \\ w_i^j + \bar{w}_{i+1}^j \\ \frac{1}{2}|\nabla\phi_i^j|^2 + \frac{1}{2}|\nabla\bar{\phi}_{i+1}^j|^2 + 2\frac{P_\infty - P_g}{\rho} \end{Bmatrix} \quad (15)$$

where the superscript refers to the nodes and the subscript refers to the time step. The value of  $|\nabla\phi|$  is computed from the derivative of  $\phi$  in the direction normal to the bubble surface, which, in turn, is obtained from the solution of the integral equation, and the derivative in the direction tangent to the surface, obtained from a central difference scheme.

In the numerical solution of the integral equation (Eq. 8), the values of  $\phi$  and  $\partial\phi/\partial n$  are assumed to vary linearly in the  $\theta = 0$  plane as the source point is varied along each panel. The integral equation in its discrete form can be written as

$$\alpha^i \phi^i = \sum_{j=1}^N \left( G^{1,i,j} \left( \frac{\partial\phi}{\partial n} \right)^j + G^{2,i,j} \left( \frac{\partial\phi}{\partial n} \right)^{j+1} \right)$$

$$-\sum_{j=1}^N (GN^{1,i,j} \phi^j + GN^{2,i,j} \phi^{j+1}) \quad (16)$$

where  $N = n_e + n_w$  and

$$\begin{aligned} G^{1,i,j} &= \int_0^{L^j} r(l^j) \frac{L^j - l^j}{L^j} \int_0^{2\pi} \frac{1}{|\vec{p}^i - \vec{q}^j(r, \theta)|} d\theta dl^j \\ G^{2,i,j} &= \int_0^{L^j} r(l^j) \frac{l^j}{L^j} \int_0^{2\pi} \frac{1}{|\vec{p}^i - \vec{q}^j(r, \theta)|} d\theta dl^j \\ GN^{1,i,j} &= \int_0^{L^j} r(l^j) \frac{L^j - l^j}{L^j} \int_0^{2\pi} \frac{\partial}{\partial n} \left( \frac{1}{|\vec{p}^i - \vec{q}^j(r, \theta)|} \right) d\theta dl^j \\ GN^{2,i,j} &= \int_0^{L^j} r(l^j) \frac{l^j}{L^j} \int_0^{2\pi} \frac{\partial}{\partial n} \left( \frac{1}{|\vec{p}^i - \vec{q}^j(r, \theta)|} \right) d\theta dl^j . \end{aligned}$$

In these equations, the length of panel  $j$  in the  $\theta = 0$  plane is given by  $L^j$ , and  $l^j$  is the distance coordinate along the panel. The parameter  $\alpha^i$  is the solid angle within the fluid subtended by the fluid surface at node  $i$ . The integrations in the  $\theta$ -direction were carried out analytically following the method of Jaswon and Symm<sup>15</sup>; results in terms of elliptic integrals were obtained. The integrations in  $l^j$  were carried out numerically using Gauss-Legendre quadrature techniques for the regular parts of the integrals and the quadrature methods of Anderson<sup>16</sup> for the singular parts of the integrals.

The structural finite element program, developed by Whang<sup>17</sup>, has been modified to include isoparametric continuum elements and Newmark-Beta (see Newmark<sup>18</sup>) time integration with variable time step size. The structure is discretized into  $n_e$  quadrilateral finite elements, interconnected at  $n_s$  nodal points. Each element is comprised of four nodes. For each structural node on the fluid-structure interface there is a corresponding node in the fluid model. Coupling of the fluid and structural models is accomplished by exchanging pressure and velocity information between these pairs of fluid and structural nodes. The numerical forms of the boundary conditions at the flow-structure interface (Eqs. 6 and 7) are

$$\left[ \frac{\partial \xi_n}{\partial t} \right]_i^{j_s} = - \left[ \frac{\partial \phi}{\partial n} \right]_i^{j_f} \quad (17)$$

$$P_{i+1}^{j_s} - P_\infty = P_{i+1}^{j_f} - P_\infty = \rho \frac{\phi_{i+1}^{j_f} - \phi_i^{j_f}}{t_{i+1} - t_i} \quad (18)$$

where  $\left[\frac{\partial \xi_n}{\partial t}\right]_i^{j_s}$  is the normal velocity of structural node  $j_s$ , and  $\left[\frac{\partial \phi}{\partial n}\right]_i^{j_f}$  is the normal derivative of the velocity potential at the corresponding fluid node  $j_f$ . The second boundary condition merely states that the pressure computed at fluid node  $j_f$  is applied at the corresponding structural node  $j_s$ .

The time step of the calculation varied during each run. At each step, the time difference

$$\Delta t_v = \frac{\Delta \Phi_{max}}{1 + 0.5q_{max}^2}$$

was computed, where  $\Delta \Phi_{max}$  is a constant and  $q_{max}$  is the maximum fluid velocity on the surface of the bubble at any time step. A minimum time step,  $\Delta t_{min}$ , and a maximum time step,  $\Delta t_{max}$ , were chosen such that  $\Delta t_{min} = \Delta t_{max}/200$ . If  $\Delta t_{min} < \Delta t_v < \Delta t_{max}$ , then  $\Delta t_v$  was used as the time step. If  $\Delta t_v > \Delta t_{max}$  the time step was taken as  $\Delta t_{max}$ , while if  $\Delta t_v < \Delta t_{min}$ , the time step was taken as  $\Delta t_{min}$ .

## PROGRAM VERIFICATION

A series of interactive calculations was performed to assess the overall performance of the coupled flow and structural algorithms. This was accomplished by making direct comparisons between the results of the present model, employing the finite element method and the results of Duncan and Zhang's model, using the finite difference method. The calculations simulated the collapse of a bubble near a spring-backed membrane.

## MODEL DESCRIPTIONS

A schematic showing an idealization of a spring-backed membrane and a vapor bubble is given in Fig. 4. The spherical bubble is initially at rest with radius  $R_o$  and is centered at  $r = 0$ ,  $z = Z_o$ . The pressure inside the bubble,  $P_o$ , and the pressure in the fluid at infinity,  $P_\infty$ , are held constant during the calculation. The membrane lies in the  $r$ - $\theta$  plane and is centered at  $r = 0$ ,  $z = 0$ . The membrane has radius  $R_m$ . For  $r > R_m$  on  $z = 0$ , the boundary is modeled as a flat rigid wall. A constant tensile force,  $T$ , is applied to the membrane at  $r = R_m$ .

The finite difference membrane has three independent variables, mass per unit area,  $m$ ; spring constant per unit area,  $K$ ; and membrane tension per unit length,  $T$ . The independent variables for the flow are the initial radius of the bubble,  $R_o$ , the initial standoff from the bubble to the membrane,  $Z_o$ , the pressure difference,  $\Delta P = P_\infty - P_o$ , and the density of the fluid,  $\rho_f$ . From this set of eight independent variables, several dimensionless parameters can be formed that relate the properties of the membrane to the conditions in the fluid. The parameters include the dimensionless inertia,  $M^*$ , spring constant,  $K^*$ , and membrane tension,  $T^*$ . The parameters are defined as follows:

$$M^* = \frac{m}{\rho_f R_o} \quad (19)$$

$$K^* = \frac{K R_o}{\Delta P} \quad (20)$$

$$T^* = \frac{T}{R_o \Delta P} \quad (21)$$

$M^*$  is the ratio of the mass per unit area of the membrane to an equivalent mass per unit area of the fluid based on thickness  $R_o$ .  $K^*$  and  $T^*$  are the ratios of the spring and tension terms, respectively, in the membrane model to the pressure driving the collapse. In order to obtain relevant comparisons between the finite element and finite difference results, it is necessary to identify finite element equivalents for the dimensionless parameters  $M^*$ ,  $K^*$ , and  $T^*$ .

The finite element idealization of the spring-backed membrane is shown schematically in Fig. 5. There are 20 elements in the radial direction and the membrane is one-element thick. The length of each element is the same as that of the corresponding flow panels, i.e.,  $0.125 R_o$ . Symmetry conditions require that all nodes at  $r = 0$  be constrained from moving in the radial direction. The nodes on the edge of the membrane at  $r = R_m$  are constrained from moving vertically. All nodes along the base of the backing elements,  $z = -(t_m + t_b)$ , are fixed in both the radial and vertical directions.

A very thin finite element membrane is required to minimize bending stiffness and mass distribution effects that are not present in the finite difference model. However, finite element aspect ratio considerations require that

the element thickness be no less than one fourth of the in-plane dimension. Thus, a membrane thickness,  $t_m$ , of  $t_m = 0.125 R_o/4 = R_o/32$  is used. The spring backing is modeled with two rows of square elements and has a total thickness  $t_b$ . The axial stiffness per unit area of the backing elements is obtained from generalized Hooke's law (Timoshenko and Goodier<sup>19</sup>), which in this case reduces to the following:

$$K = \frac{E}{t} \quad (22)$$

where  $K$  is the spring constant per unit area,

$E$  is Young's modulus of the specimen, and

$t$  is the thickness of the specimen in the direction of the applied load.

The combined axial stiffness per unit area,  $K_t$ , of the membrane and spring backing is obtained by treating the two layers as a set of springs in series, i.e.,

$$K_t = \left[ \frac{t_m}{E_m} + \frac{t_b}{E_b} \right]^{-1} \quad (23)$$

where  $E_m$  and  $E_b$  are the Young's moduli of the membrane and backing elements, respectively. The Young's modulus of the backing elements,  $E_B$ , is chosen so that the axial stiffness per unit area of the backing provides the required spring constant,  $K$ . A Young's modulus for the membrane is chosen such that  $\frac{E_m}{t_m} \gg \frac{E_b}{t_b}$ . Consequently, the axial stiffness of the membrane,  $\frac{E_m}{t_m}$  has a negligible effect on the combined axial stiffness of the membrane and backing. The combined axial stiffness per unit area of the system is now

$$K_t = \frac{E_b}{t_b}. \quad (24)$$

For the finite element case, the mass per unit area,  $m$ , is

$$m = \rho_m t_m + \rho_b t_b \quad (25)$$

where  $\rho_m$  is the density of the membrane and  $\rho_b$  is the density of the backing. The density of the backing elements is chosen so that  $\rho_b t_b \ll \rho_m t_m$ ; hence,

the mass per unit area reduces to  $m = \rho_m t_m$ . The finite element equivalents for  $M^*$  and  $K^*$  are expressed as

$$M^* = \frac{\rho_m t_m}{\rho_f R_o} \quad (26)$$

$$K^* = \frac{K_t R_o}{\Delta P} = \frac{E_B R_o}{t_B \Delta P}. \quad (27)$$

The finite element equivalent for  $T^*$  is the same as for the finite difference model, i.e.,  $T^* = \frac{T}{R_o \Delta P}$ .

## COMPARISON OF RESULTS

In the calculations described in this section, the bubble is represented by 20 panels of equal arc length. The membrane radius is  $2.5 R_o$  and the flow-membrane interface is represented by 20 panels of length  $0.125 R_o$ . The rigid portion of the flow boundary surrounding the membrane is modeled with 40 panels of increasing length, so that the last node is at  $r = 100 R_o$ . This flow discretization is used in both the finite difference and finite element calculations. The following values are held constant in both sets of calculations to be discussed later;  $\Delta P = 1.0$ ,  $\rho_f = 1.0$ , and  $Z_o = 1.5 R_o$ . Furthermore, the calculations are for the collapse phase of the interaction only; hence  $R_o = R_{max} = 1.0$ . In the finite element calculations, Poisson's ratio for the spring backing  $\nu_b$  and that of the membrane  $\nu_m$  are taken as zero.

Figure 6 contains plots of the membrane velocity at  $r = 0.0$  for  $M^* = K^* = 2.0$ . The results of the finite difference and finite element membrane models are very similar. In both cases the velocity reaches a maximum at roughly two thirds the overall collapse time and decreases rapidly at the end of the collapse. In Fig. 7, the pressure difference ( $P_m - P_\infty$ ) on the membrane at  $r = 0.0$  is plotted for  $M^* = K^* = 2.0$ . The pressure remains constant for most of the collapse and then increases very rapidly towards the very end of the collapse. For this reason, it is most informative to plot the pressure versus the vertical separation of the north and south poles of the bubble. Once again the finite element membrane results are in close agreement with the results of Duncan and Zhang's model. The pressure on the membrane increases gradually for most of the collapse and then rises rapidly when the

separation of the poles of the bubble has reached about 20 percent of its original value.

The excellent agreement between the results of the two interaction models provides a good indication that the coupled finite element/boundary element model is working properly.

## COMPARISON WITH EXPERIMENTAL DATA

The most extensive set of experimental data on the behavior of vapor cavities near compliant walls, is that published by Shima et al.<sup>9</sup> What follows is a description of an attempt to simulate this experimental work numerically.

### DESCRIPTION OF EXPERIMENT

Figure 8 shows a schematic of the experimental set-up. The experiments were conducted in a stainless steel bubble chamber containing tap water at atmospheric pressure and room temperature. A composite surface was placed in contact with the free surface of the water, and a vapor bubble was then generated by means of electric spark discharge. The growth and subsequent collapse of the bubble was recorded photographically. Composite wall properties such as inertia and stiffness were varied, and their effect on collapse behavior was observed.

The composite surface was 40 mm in diameter and consisted of a Nitrile rubber sheet of thickness,  $t_r$ , and a foam rubber backing of thickness,  $t_f$ . The foam rubber density,  $\rho_f$ , was  $0.024 \text{ g/cm}^3$ , and the Nitrile rubber density,  $\rho_r$ , was  $1.39 \text{ g/cm}^3$ . A series of uniaxial compression tests was performed to determine the axial stiffness of the individual layers. It was observed that for  $5 \text{ mm} < t_f < 20 \text{ mm}$ , the spring constant,  $K_f$ , for the foam rubber was  $3.0 \text{ kg/cm}$ . For the Nitrile rubber, the value  $K_r = 8.3 \text{ kg/cm}$  was reported for a specimen with thickness  $t_r = 5 \text{ mm}$ . A set of dimensionless parameters was used to describe the composite surface. The parameters were the dimensionless surface inertia,  $M^*$ , and dimensionless surface stiffness,  $K^*$ ,

defined as follows:

$$M^* = \frac{\rho_r t_r + \rho_f t_f}{\rho_l R_{max}} \quad (28)$$

$$K^* = \frac{K_t R_{max}}{P_\infty - P_o} \quad (29)$$

where  $K_t$  is the combined stiffness of the foam and Nitrile rubber layers ( $K_t = \left[\frac{1}{K_f} + \frac{1}{K_r}\right]^{-1}$ ),  $P_\infty$  is the pressure in the water at infinity,  $P_o$  is the pressure inside the bubble (vapor pressure of the water),  $\rho_l$  is the density of the water, and  $R_{max}$  is the maximum bubble radius. In this case ( $P_\infty - P_o$ ) = 1.0159 and  $R_{max} = 3.5$  mm. The thickness of the foam rubber was held constant ( $t_f = 20$  mm). Variation of the composite wall stiffness and inertia was obtained by varying the thickness of the Nitrile rubber sheet between 0.3 mm and 5.0 mm.

## NUMERICAL SIMULATION

A schematic showing the numerical idealization of the experimental set-up is given in Fig. 9. The problem is axisymmetric about the z-axis. Thus the problem can be defined in the r-z coordinate plane ( $\theta = 0$ ). All lengths are normalized with respect to the maximum bubble radius,  $R_{max}$ . The pressure inside the bubble,  $P_g$ , is assumed to equal the vapor pressure of the fluid throughout the calculation, i.e.,  $P_g = P_v = const$ . The ambient fluid pressure,  $P_\infty$ , also remains constant during the calculations. Gravity effects have not been considered; thus, the vapor bubble is shown above the composite surface. The bubble is initially spherical with radius  $R_o$  and center at  $z = Z_o$ . Twenty six panels are used to model the bubble. The interface between the flow and the surface of the Nitrile rubber lies in the r- $\theta$  plane at  $z = 0$ . Flow along this surface is modeled with 40 panels of equal length. The flow boundary at  $z = 0$  is modeled as a rigid wall for  $r > R_c$ , where  $R_c$  is the radius of the compliant surface. The rigid portion of the boundary is modeled with 40 panels of increasing length so that the last node is at  $r = 100 R_{max}$ ,  $z = 0$ . The composite wall is modeled using finite elements. There are 40 elements in the radial direction, 4 elements through the thickness of the Nitrile rubber layer, and 8 elements through the foam rubber layer. (A finite element mesh

convergence study was performed for the case of  $t_r = 1.0 R_{max}$  ( $M^* = 1.4$ ).

It was concluded from this effort that the mesh density is sufficient to model this thickness of Nitrile rubber.) Nitrile and foam rubber densities are as stated in the previous section. Young's moduli for the two materials are obtained from the spring constant data for the individual layers. Applying generalized Hooke's law (Timoshenko and Goodier<sup>19</sup>) to the loading and boundary conditions of the uniaxial compression tests, yields the following relation between Young's modulus and axial stiffness

$$K = \frac{AE}{t} \quad (30)$$

where  $K$  is the spring constant for the Nitrile or foam rubber,

$A$  is the cross sectional area of the rubber specimen,

$t$  is the thickness of the rubber, and

$E$  is the Young's modulus of the material.

Solving the above relation for  $E$  yields Young's modulus of 0.330 kPa and 0.120 kPa for the Nitrile and foam rubbers, respectively. Poisson's ratio for the two materials was not provided. Nitrile rubber is nearly incompressible, and a Poisson's ratio,  $\nu_r$ , of 0.49 is routinely used for the treatment of rubber materials in finite element analysis. Conversely, the foam rubber is quite compressible, and the Poisson's ratio for the material is probably not a constant. A review of data for other foam rubber materials indicates a range of Poisson's ratio between 0.24 and 0.36. Lacking further information on this particular material, a Poisson's ratio of  $\nu_f = 0.30$  is assumed. It is important to note that these material properties were obtained from static stiffness measurements. However, strain rates cannot be expected to remain near quasi-static values throughout the entire fluid-structure interaction. Poisson's ratio and Young's modulus for many rubber and foam materials are sensitive to the rate at which the load is applied (Hunston, Yu, and Bullman<sup>20</sup>). Thus, the statically measured values for Young's modulus and Poisson's ratio may not accurately characterize the composite wall materials throughout the entire time domain of interest.

## COMPARISON OF RESULTS

An interesting parameter describing the collapse of the bubble is the collapse height,  $z_c$ . Collapse height is the height above the composite surface where the north and south poles of the bubble meet at the end of the collapse. In the published experimental data, the collapse height is presented in plots of  $z_c$  versus the dimensionless surface inertia  $M^*$ . Variation in  $M^*$  is achieved by changing the thickness of the Nitrile rubber layer while holding the thickness of the foam rubber layer constant. Comparative data are obtained by performing a series of calculations in which the thickness of the Nitrile rubber elements in the finite element model is varied. Note that as the thickness of the Nitrile layer is increased, the number of elements in the structural model increases also, while mesh density remains more or less invariant. The results of the numerical study along with the experimental data for initial standoffs  $Z_o = 1.14 R_{max}$ ,  $Z_o = 1.43 R_{max}$  and  $Z_o = 1.71 R_{max}$  are presented in Figs. 10 through 12, respectively. For the case of  $Z_o = 1.14 R_{max}$  (Fig. 10), the calculated values of collapse height are shifted towards higher  $M^*$  for  $M^* < 1.75$ . The slopes of the calculated and experimental curves differ for low  $M^*$ . However, at higher values of  $M^*$  the asymptotic behavior of the two curves seems to be similar. For the case of  $Z_o = 1.43 R_{max}$  (Fig. 11), there is good agreement between the experimental results and the present calculations. For  $M^* < 1.75$ , the shapes of the two curves are about the same, with the calculations shifted to slightly larger  $M^*$ . For  $M^* > 1.75$ , the calculated collapse height drops off more rapidly than for the experimental data. This behavior could be an indication that the finite element program is underpredicting the response of the composite surface and causing the interaction calculation to tend toward the rigid wall case more rapidly than it should as  $M^*$  is increased. The collapse height predictions for  $Z_o = 1.71 R_{max}$  (Fig. 12) are slightly higher than the experimentally observed values; however, the shapes of the two curves are similar.

There are several possible sources of discrepancy between the experimental results and the calculations. In the calculations, the pressure inside the bubble was held constant at the fluid vapor pressure. In the experiment, there was evidence of burning of electrode material during the spark generation process. The compressibility of the gaseous products resulting from

electrode burning is likely to have affected the experimental results. The inadequacy of the linear elastic material model to represent the Nitrile rubber is likely to be a major source of error in the calculations. A strain-rate sensitive nonlinear elastic representation of the rubber properties is a necessity in these calculations. Finally, the linearized boundary condition on the fluid-structure interface is likely to have influenced the predictions for low  $M^*$ . In these cases, the Nitrile surface attains a significant normal velocity, but this was not considered in the linearized Bernoulli equation.

## INTERACTION WITH A COMPLIANT SPHERE

### MODEL DESCRIPTION

The interaction calculations discussed thus far have involved planar fluid-structure interfaces, constant bubble internal pressure, and no gravitational effects. Attention is now focused on a more complex problem involving a doubly-curved fluid-structure interface, namely, the interaction between a growing and collapsing bubble and a submerged spherical structure. The problem is shown schematically in Fig. 13. The problem is rotationally symmetric and is defined in cylindrical coordinates ( $r$ - $z$ ) at  $\theta = 0$ . The  $z$ -axis pierces the north and south poles of both bubble and sphere. The spherical structure has outer radius  $R_s$ , wall thickness  $t_s$  and is centered at  $r = 0$ ,  $z = -R_s$ . By requiring the spherical structure to be thin walled,  $\frac{R_s}{t_s} > 50$ , thin shell theory can be used to validate the structural portion of the model. As in the previous calculations, the bubble is initially spherical with radius  $R_o$  and center at  $r = 0$ ,  $z = Z_o$  (the center of the bubble is initially at depth  $d$  below the fluid free surface) and the pressure inside the bubble is initially  $P_{g0}$ . Bubble internal pressure is made to obey the polytropic law,  $P_g = P_{g0} \left(\frac{V_0}{V}\right)^\gamma$ , where  $V_0$  is the initial bubble volume and  $V$  is the instantaneous bubble volume. The bubble is modeled with 30 flow panels and the "wet" shell interface is modeled with 60 panels. The structural finite element model has 60 meridional elements and one element through the shell thickness (Fig. 14). The structural nodes on the axis of symmetry are prevented from moving radially but are free to move in the vertical direction. Thus the spherical structure can undergo rigid body vertical motion, as well as local

deformation.

There are 10 independent variables in this interaction problem. For the flow, the variables are the initial pressure differential,  $\Delta P = P_{g0} - P_{\infty}$ ; fluid density,  $\rho_f$ ; initial position of the bubble,  $Z_0$ ; initial radius of the bubble,  $R_0$ ; and maximum bubble radius,  $R_{max}$ . For the spherical structure, the variables are the outer radius,  $R_s$ ; wall thickness,  $t_s$ ; Young's modulus,  $E_s$ ; Poisson's ratio,  $\nu_s$ ; and density of the structural material,  $\rho_s$ . An interesting parameter in this problem is the collapse height,  $z_c$ , which is the height above the north pole of the sphere where the north and south poles of the bubble meet at the end of the collapse. Collapse height is a function of the 10 independent variables previously discussed, but can be expressed in terms of seven dimensionless parameters

$$\frac{z_c}{Z_0} = f \left( \frac{R_0}{R_{max}}, \frac{R_s}{R_{max}}, \frac{t_s}{R_s}, \frac{Z_0}{R_{max}}, \frac{\rho_s (R_s^3 - R_i^3)}{\rho_f R_{max}^3}, \frac{K}{R_{max} \Delta P}, \frac{B}{R_{max}^3 \Delta P} \right) \quad (31)$$

where  $R_i$  is the inner radius of the shell ( $R_i = R_s - t_s$ ),

$K$  is its extensional rigidity (Kraus<sup>21</sup>),  $K = \frac{2E_s t_s}{(1-\nu_s)}$ , and

$B$  is its bending rigidity (Timoshenko and Woinowsky-Krieger<sup>22</sup>)

$$B = \frac{E_s t_s^3}{12(1-\nu_s^2)}.$$

For ease of reference, the last three shell terms on the right-hand side of Eq. 31, are defined as  $M^*$ ,  $K^*$ , and  $B^*$ , respectively.  $M^*$  is the mass ratio of the sphere to the displaced fluid at  $R_{max}$ . The dimensionless membrane stiffness,  $K^*$ , is the ratio of the extensional stiffness to the pressure driving the collapse. The dimensionless flexural stiffness,  $B^*$ , relates bending stiffness to the pressure driving the collapse. In this study, the outer radius of the spherical structure is a multiple of  $R_{max}$ ;  $R_s = nR_{max}$ . Thus,  $B^*$  can be expressed in terms of the radius of the shell

$$B^* = \frac{n^3}{12} \frac{E}{(1-\nu^2)} \left( \frac{t_s}{R_s} \right)^3 \frac{1}{\Delta P}. \quad (32)$$

It should be noted that since  $R_s/t_s > 50$  and  $1 \gg (t_s/R_s)^3$ , the bending stiffness of the sphere is relatively small and its influence here is negligible.

## RESULTS

The time scale for the flow in this problem is  $T_o = R_{max} \sqrt{\frac{\rho_f}{P_\infty}}$ . In the calculations that are described in this section, all times and lengths are nondimensionalized by  $T_o$  and  $R_{max}$ , respectively. Furthermore,  $\rho_f$ ,  $P_\infty$ , and  $R_{max}$  are taken as unity in their respective units;  $\gamma = 1.25$ ;  $Z_o = 1.5 R_{max}$  and the calculations begin with the bubble radius  $R_o = 0.4 R_{max}$ . The initial bubble internal pressure is  $P_{g_o} = 1.5 P_\infty$ . The bubble's initial conditions have been chosen to be consistent with the detonation of one half pound of TNT at a depth of 300 ft (see Cole<sup>3</sup> for a detailed discussion of the gas globe that results from the detonation of TNT). The structure has radius  $R_s = 4 R_{max}$  and wall thickness,  $t_s = 0.075 R_{max}$  so that  $R_s/t_s = 53.33$ . For now, gravitational and depth effects are not included in the calculations. The ambient hydrostatic pressure,  $P_\infty$ , is applied statically to the structure at the start of the transient calculation. The resulting hydrostatic displacements are part of the initial conditions for the structure in the subsequent dynamic calculation. The deformation of the shell due to this static preload must be small since the boundary conditions are satisfied at the undisturbed position of the fluid-structure interface. This condition dictates a fairly stiff shell (high  $K^*$ ); hence, Young's modulus for the sphere is fixed at  $E_s = 10,000.0 P_\infty$ . The resulting value of  $K^*$  is then 4286, and the static deflection due to  $P_\infty$  is  $\delta = t_s/10.0$  for Poisson's ratio  $\nu_s = 0.30$ .

We now consider the effect of  $M^*$  on the collapse of the bubble while holding fixed all other dimensionless parameters and again neglecting gravitational effects. Variation in  $M^*$  is achieved by changing the density of the structural material. Figure 15 contains plots of the height of the north and south poles of the bubble as a function of time. The plots are for four different values of  $M^*$  and for the case in which the sphere is rigid and fixed in space. The height at which the poles of the bubble meet is indicated by a short dashed line. In the rigid sphere case, the collapse height is  $z_c = 0.966 R_{max}$ , and the total time for the growth and collapse is  $t_c = 1.856 T_o$ . For a flat rigid wall with  $R_o = 0.4 R_{max}$  and  $Z_o = 1.5 R_{max}$ , the collapse height is  $z_c = 0.85 R_{max}$ , and the collapse time is  $t_c = 2.024 T_o$ . Thus, adding curvature to the fluid-structure interface significantly alters the dynamic behavior

of the bubble. When the sphere is compliant but very massive ( $M^* = 226$ ), the collapse time is  $t_c = 2.104 T_o$ , and the collapse height is  $z_c = 0.865 R_{max}$ . Reducing the dimensionless mass of the sphere to  $M^* = 92$  yields  $t_c$  and  $z_c$  values of  $2.104 T_o$ , and  $1.16 R_{max}$ , respectively. As  $M^*$  is decreased further, the collapse height increases monotonically, and the collapse time decreases. At these lower values of  $M^*$ , the poles of the bubble do not meet at the end of the collapse calculation. This is an indication that the collapse has become almost spherical. (The collapse height for a bubble collapsing spherically in an infinite fluid is  $z_c = Z_o$ .) It should be noted that in these cases of near spherical collapse, the calculation becomes unstable near the end of the collapse; hence, the final position of the bubble is a little more speculative than in the other calculations. As the mass of the sphere is reduced below  $M^* = 92$ , the separation of the poles at the end of the collapse begins to decrease, and the projected collapse height is greater than the initial standoff, indicating redirection of the bubble motion.

Profiles of the bubble at various times during the collapse near the rigid sphere and several compliant spheres of various  $M^*$  values are given in Fig. 16. In the profiles for the rigid sphere case, a reentrant jet directed toward the sphere can be seen near the end of the collapse. For  $M^* = 226$ , the later stages of collapse are also characterized by the formation of a reentrant jet directed towards the sphere. As mentioned above, the collapse height is actually smaller than the collapse height for the rigid sphere case. When  $M^*$  is reduced to 76 (Fig. 16), the collapse has been modified such that all collapse profiles are nearly spherical. The collapse height in this case,  $z_c = 1.34 R_{max}$ , is beginning to approach the value for spherical collapse in an infinite fluid,  $z_{\infty} = 1.5 R_{max}$ . When  $M^*$  is reduced to 56 (Fig. 16), the collapse height,  $z_c = 1.53 R_{max}$ , is higher than the initial standoff,  $Z_o = 1.5 R_{max}$ . In this case, deviation from sphericity is apparent. The shape of the bubble near the south pole suggests that a redirected jet is beginning to form late in the collapse.

The effect of  $M^*$  on the response of the spherical structure is illustrated in Fig. 17, which contains plots of dimensionless velocity of the north pole, in the shell normal direction (positive outward), versus time. As expected,

shell peak velocity increases as the sphere mass is reduced. Figure 18 contains similar plots for the south pole. In all cases, the south pole velocity is lower than that of the north pole, indicating that interaction between the bubble and sphere is driven by local deformation of the surface of the sphere near the bubble. North pole displacement of the shell is shown in Fig. 19 for several values of  $M^*$ . Peak displacements increase as structure mass is decreased. For  $M^* = 56$ , the peak structural displacement ( $0.066 R_{max}$ ) is nearly 90 percent of the shell thickness,  $t_s$ . Local displacements of the sphere in excess of one shell thickness violate the underlying assumptions of small displacements of the fluid-structure interface, and hence, the numerical model fails. For this reason, calculations for  $M^* < 56$  were not performed.

The effect of gravity is now included in the calculations by expressing the gravity term in Bernoulli's equation (Eq. 2) in terms of the dimensionless Froude number, i.e., Eq. (2) becomes

$$\frac{D\phi}{Dt} = \frac{1}{2} (\nabla\phi)^2 + \frac{P_\infty - P_g}{\rho_f} + \frac{(z - Z_o)}{F_r} \quad (33)$$

where all quantities are dimensionless and the Froude number is defined by  $F_r = P_\infty / \rho_f g R_{max} = d / R_{max}$  where  $d$  is the initial depth of the centroid of the bubble. Fig. 20 contains plots of the height of the north and south poles of the bubble vs time for  $M^* = 226$  and various values of  $F_r$ . When  $F_r = 206$ , i.e., the bubble is initially  $206 R_{max}$  below the fluid surface, the effect of gravity is negligible, and the collapse time and collapse height are essentially the same as for the case when gravity was not considered ( $d = 206 R_{max}$  is consistent with the initial conditions used in the previous set of calculations). As the initial bubble depth is reduced to  $100 R_{max}$ , gravitational effects have increased the collapse height to  $0.95 R_{max}$ . For the case of  $d = 10 R_{max}$ , gravitational effects have become more important than interaction forces, and the collapse height becomes greater than  $2.0 R_{max}$ . Figure 21 contains collapse profiles for  $M^* = 226$  at various depths. For the cases of  $d = 206 R_{max}$  and  $d = 100 R_{max}$ , significant target attraction and target-directed jetting occur. However, when  $d$  is reduced to  $10 R_{max}$ , the collapse is driven by gravitational effects, and the bubble migration and jetting are away from the target.

## SUMMARY

For a given initial standoff, collapse behavior near a rigid spherical target is significantly different from that near a flat rigid wall. When the sphere is very compliant, the collapse problem is sensitive to the mass of the spherical structure. When the target mass is high, a reentrant jet forms late in the collapse and is directed toward the structure. As the shell mass is decreased, the collapse becomes spherical with no jet formation. A jet, directed away from the target, begins to form when the structure mass is low. At very low structural mass, significant local shell deformation occurs, and the small displacement assumptions for the fluid-structure interface are violated. When gravitational forces are considered, the collapse is driven by interaction effects at depths greater than  $100 R_{max}$ . The collapse is driven by gravitational effects for shallow depths.

## CONCLUSION

In this study a boundary element flow algorithm was coupled with a finite element structural analyzer to perform interactive calculations of the growth and collapse of an explosion bubble near a compliant structure. The validity of the program was established through direct comparisons with a code previously developed by Duncan and Zhang,<sup>10,11</sup> in which the structure was a spring-backed membrane. There was good agreement between the results of the two programs.

Calculations of the collapse of a vapor bubble next to a composite wall were performed. The calculated collapse heights were in good agreement with published experimental data.

A parametric study of the interaction between an explosion bubble and a thin walled spherical structure was also performed. The mass of the spherical structure was found to be a critical parameter in the interaction. When the mass of the structure was high, the collapse of the bubble was characterized by the formation of a reentrant jet directed toward the structure. As the mass of the spherical structure was decreased, the collapse became spherical and no jet formed. A jet, directed away from the spherical structure, began

to form when the mass of the structure was low. Significant shell deformation, enough to violate small displacement assumptions, was associated with very low structure mass. The ratio of the depth of submergence to bubble maximum radius was also found to be a critical parameter in the collapse problem. When this ratio is large (greater than 100), the collapse is driven by interaction forces. However, for shallow submergence, gravitational effects become more important than interaction forces. For a given initial standoff, the collapse of a bubble near a rigid sphere was found to be significantly different from the case of collapse next to a rigid wall.

A promising technique has been synthesized for numerical prediction of coupled explosion bubble-structure interaction. Extension to a full three-dimensional model will make possible submarine and surface ship whipping calculations with completely interactive loading, target attraction, and buoyancy effects. This method, in combination with a shock wave fluid-structure decoupling scheme, will eventually make possible the prediction of structural response to both shock wave and hydrodynamic loading from a pulsating bubble experiencing gravity migration as well as target/free-surface attraction or repulsion.

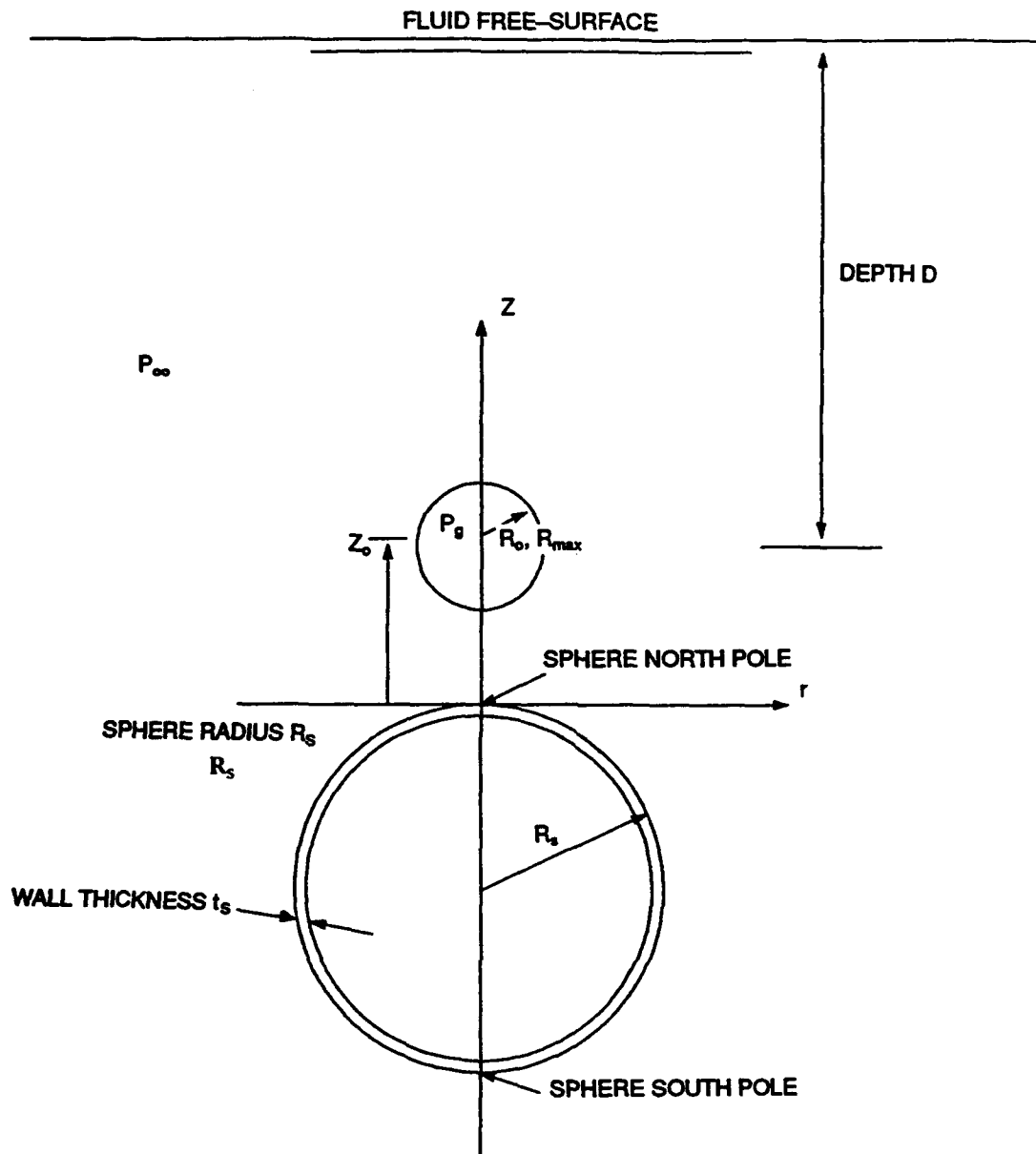


**Fig. 1.** Schematic showing the coordinate system and the initial position of the bubble and the compliant spherical shell.

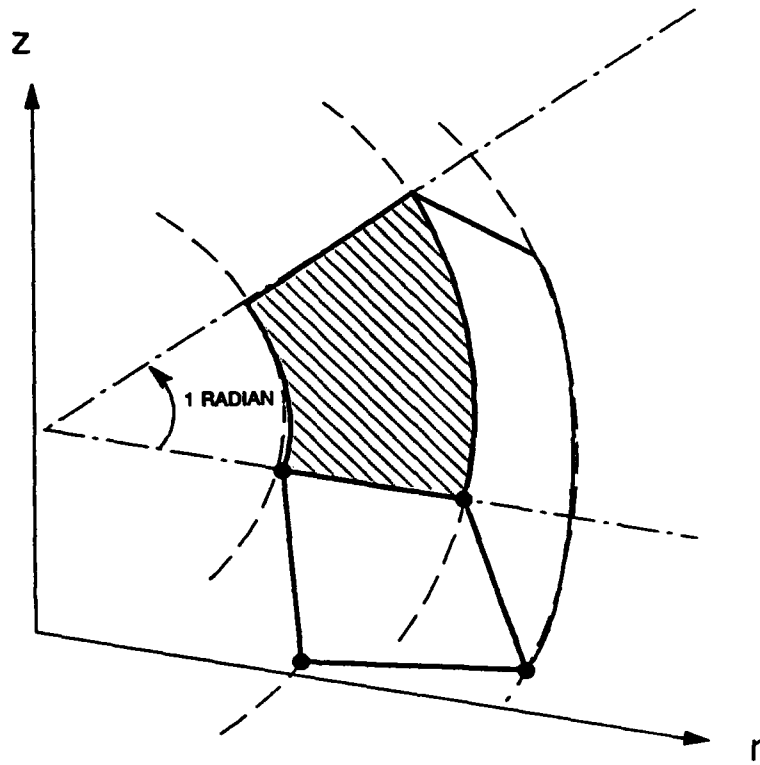


**Fig. 2.** Axisymmetric continuum element.

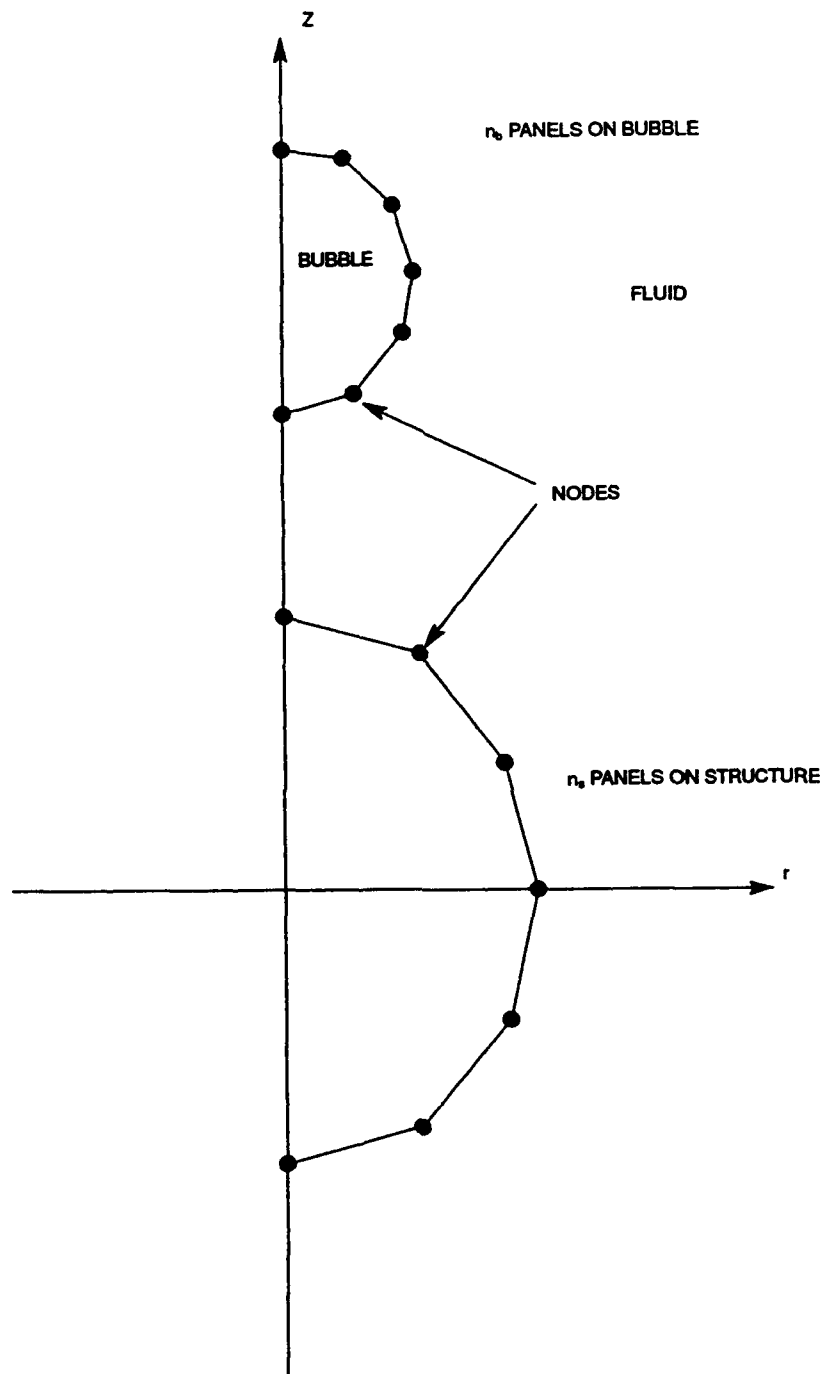


**Fig. 3.** Nodes and panels on the surface of the bubble and on the fluid-structure interface.

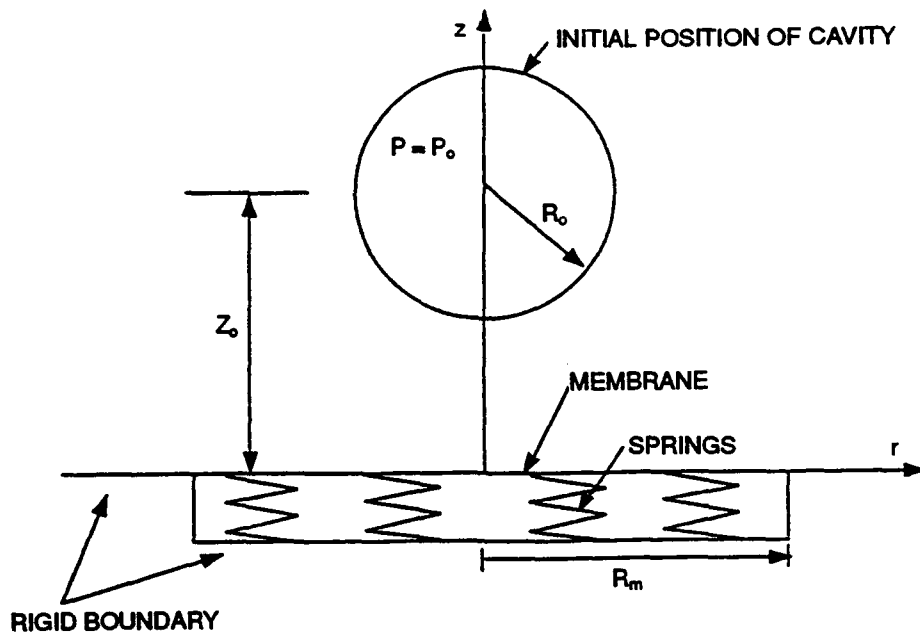


**Fig. 4.** Schematic showing spring backed membrane and initial configuration of the vapor bubble.

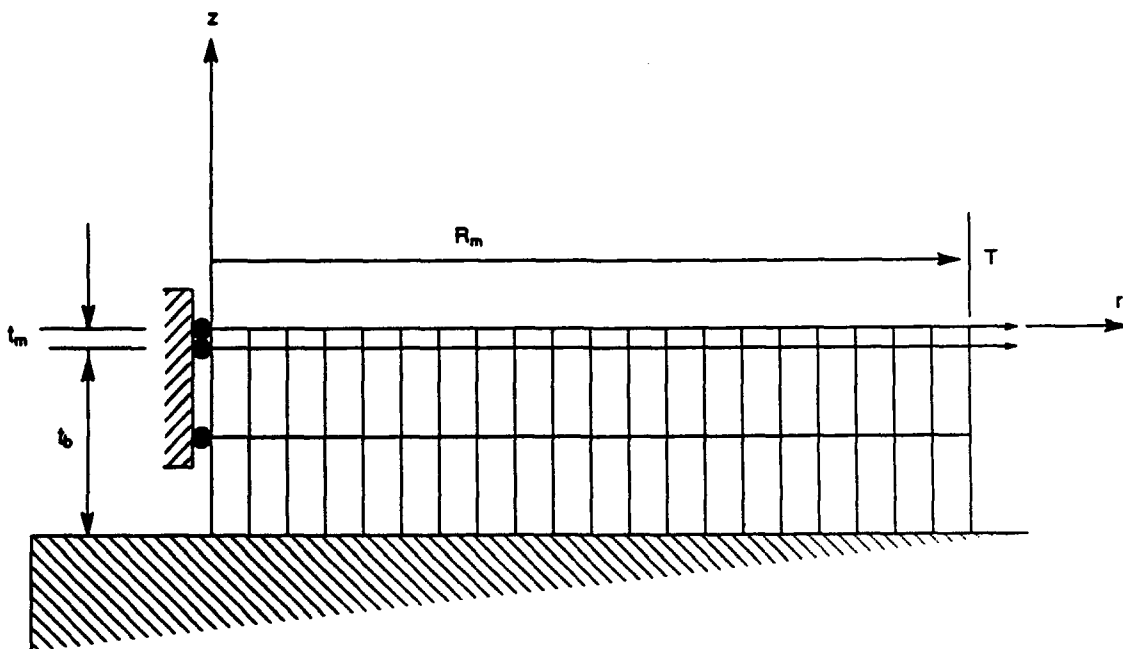


**Fig. 5.** Finite element idealization of spring backed membrane.

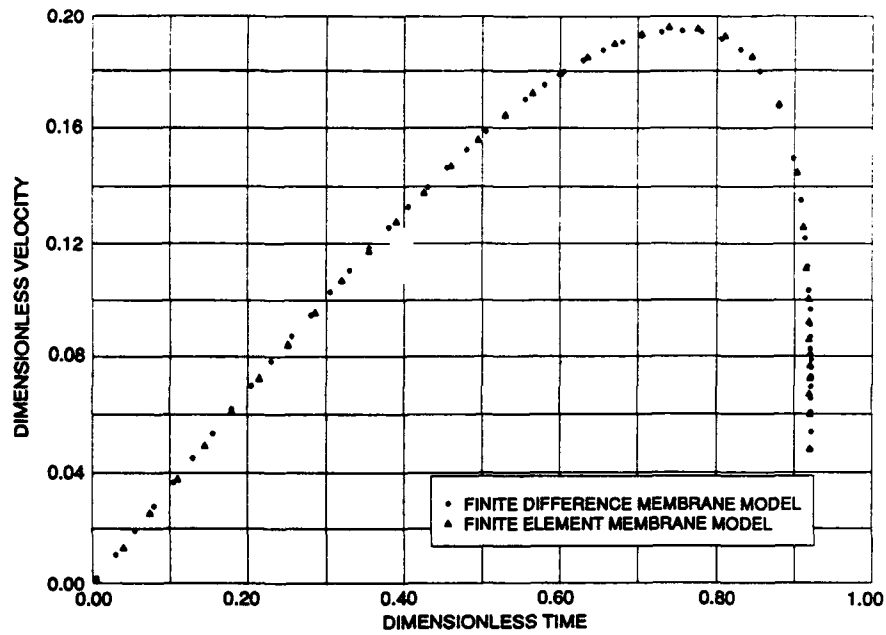


Fig. 6. Dimensionless normal velocity of membrane at  $r = 0.0$  for  $M^* = K^* = 2.0$ .

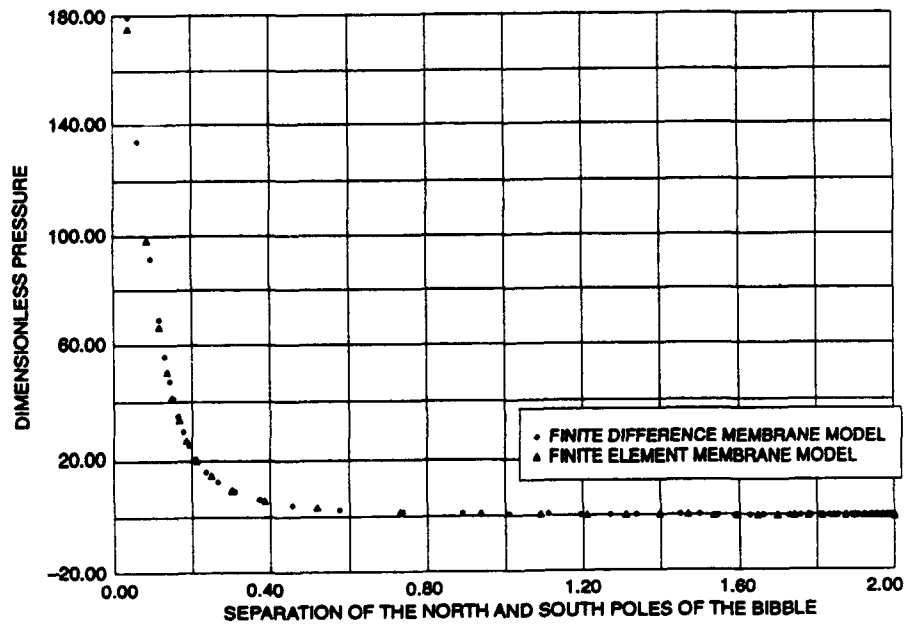
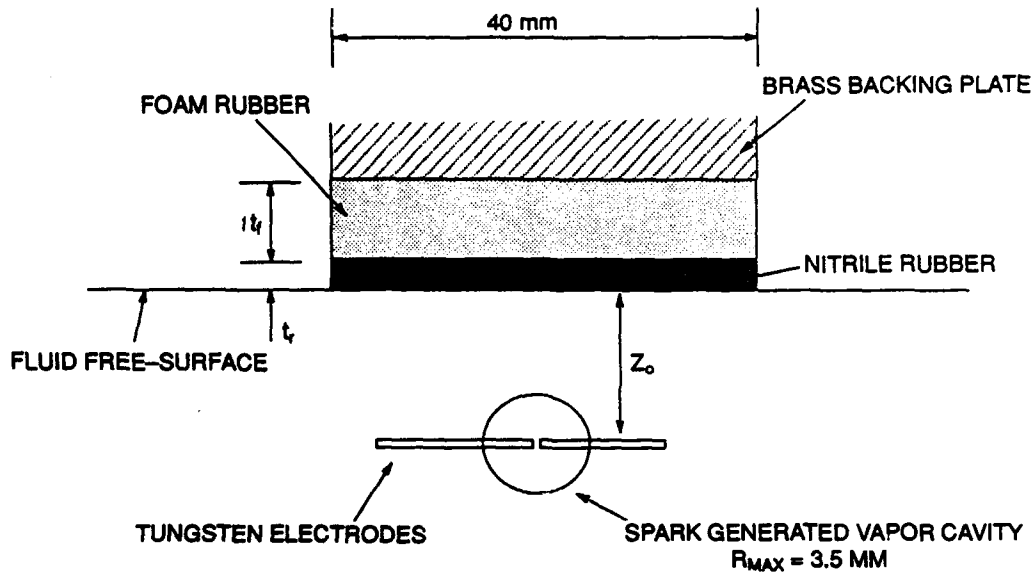
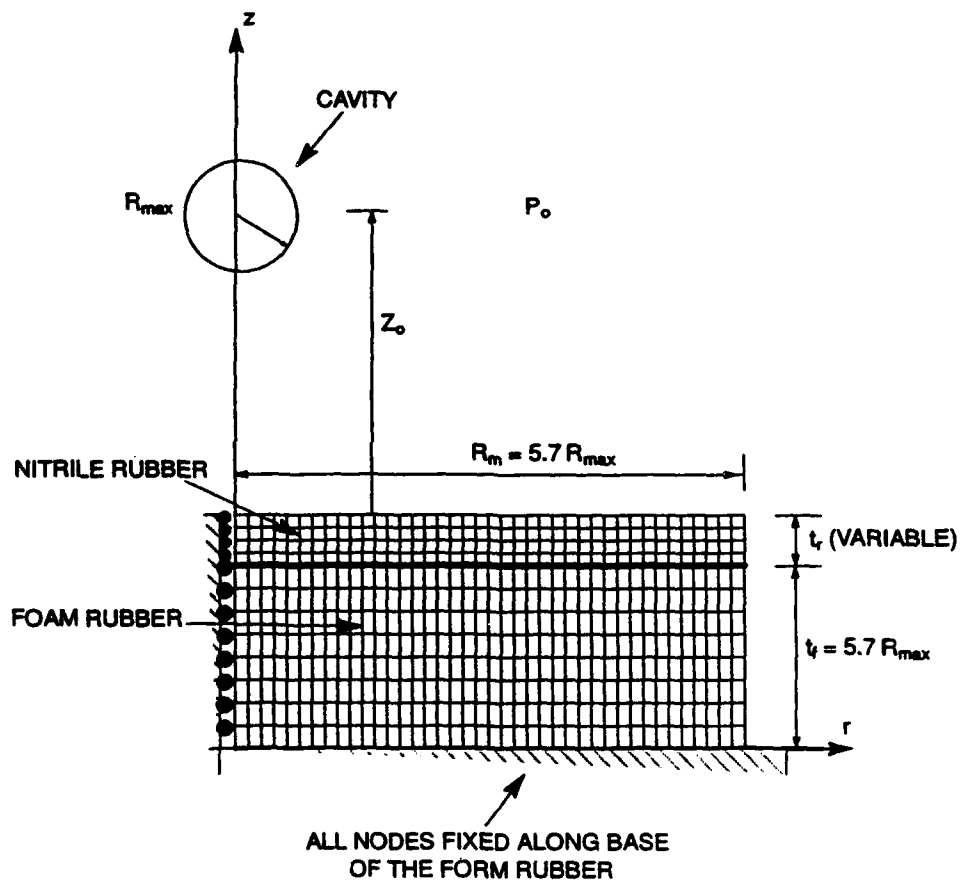


Fig. 7. Dimensionless pressure  $P_m/\Delta P$  on membrane at  $r = 0.0$  versus separation of north and south poles of the bubble  $(z_{np} - z_{sp})/R_{max}$  for  $M^* = K^* = 2.0$ .



**Fig. 8.** Schematic showing experimental set-up for compliant coating experiments of Shima, Tomita, Gibson, and Blake.



**Fig. 9.** Finite element idealization of compliant coating.

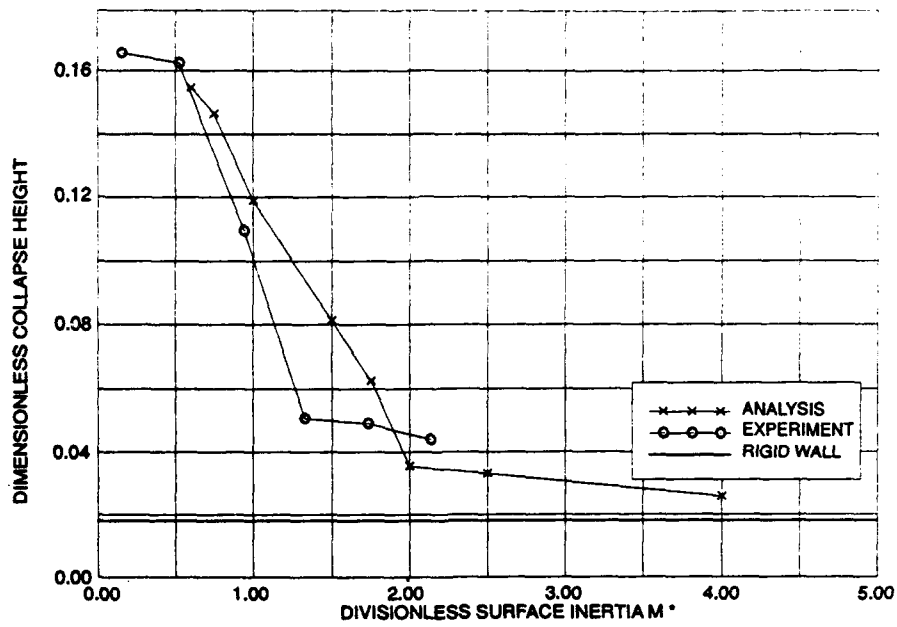


Fig. 10. Comparison of results of present calculations and data from experiments of Shima, Tomita, Gibson and Blake. Plot of  $z_c/R_{max}$  versus  $M^*$  for  $Z_0 = 1.14 R_{max}$ .

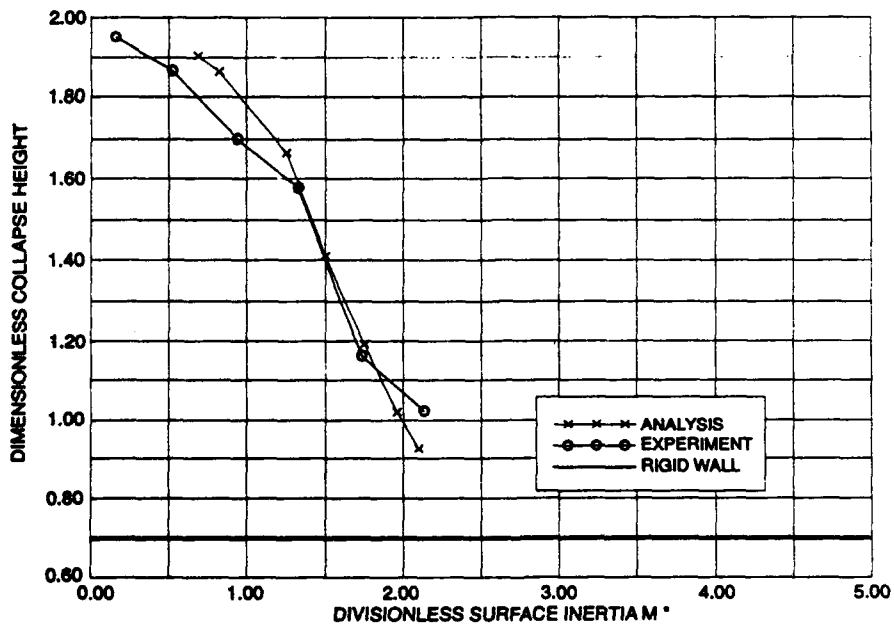
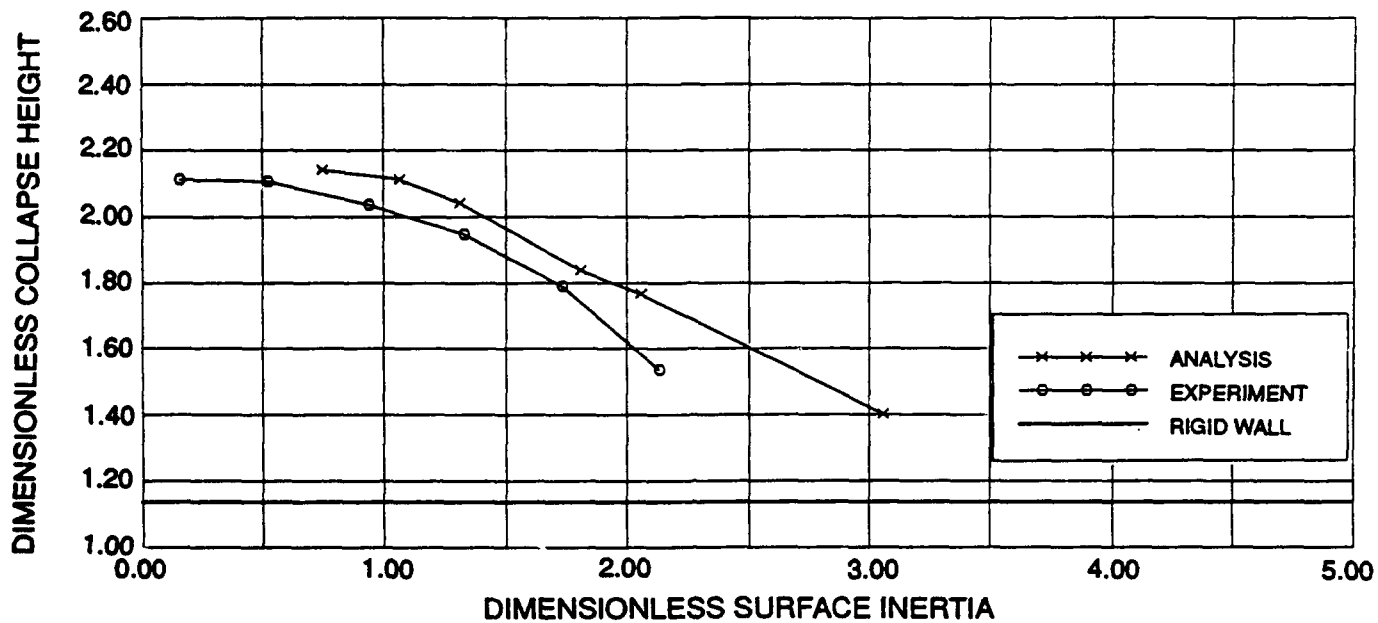
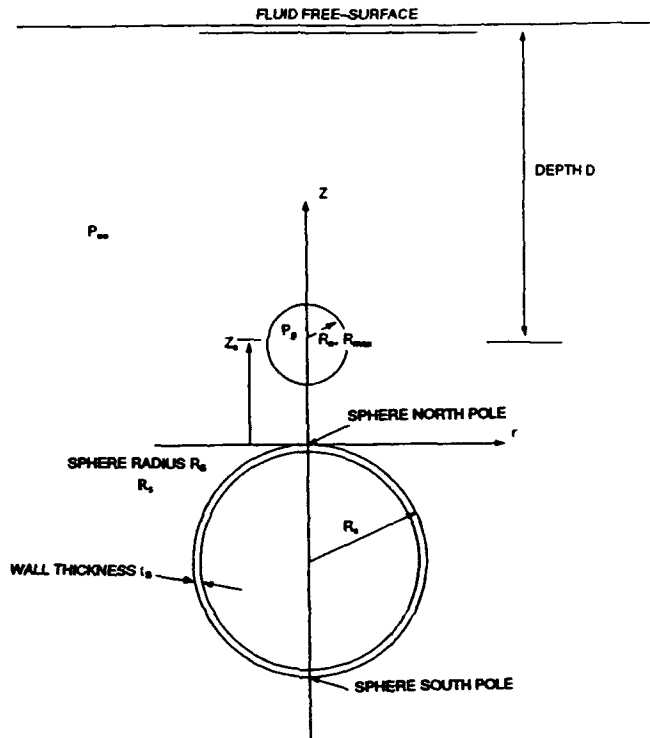


Fig. 11. Comparison of results of present calculations and data from experiments of Shima, Tomita, Gibson and Blake. Plot of  $z_c/R_{max}$  versus  $M^*$  for  $Z_0 = 1.43 R_{max}$ .



**Fig. 12.** Comparison of results of present calculations and data from experiments of Shima, Tomita, Gibson and Blake. Plot of  $z_c/R_{max}$  versus  $M^*$  for  $Z_o = 1.71 R_{max}$ .



**Fig. 13.** Schematic showing coordinate system, spherical shell, and initial position of the explosion bubble.

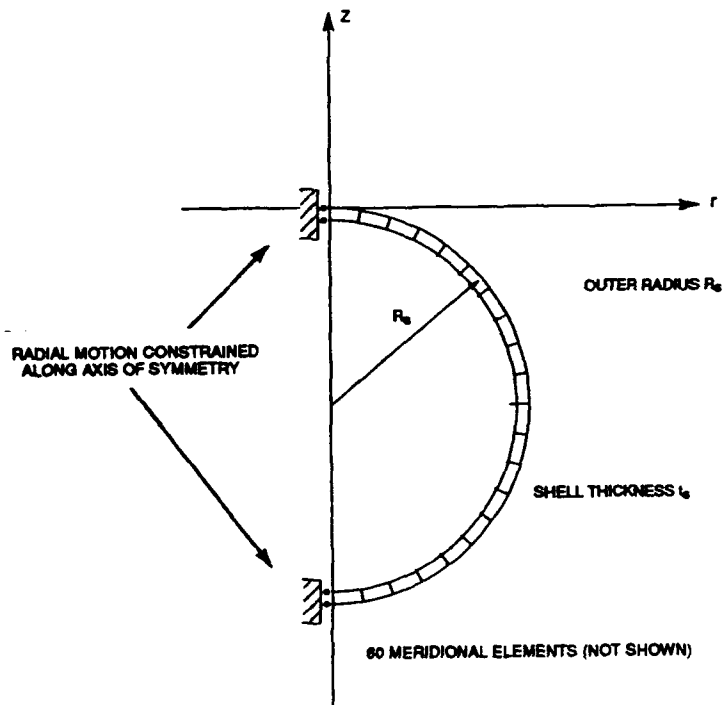


**Fig. 14.** Finite element idealization of spherical shell.

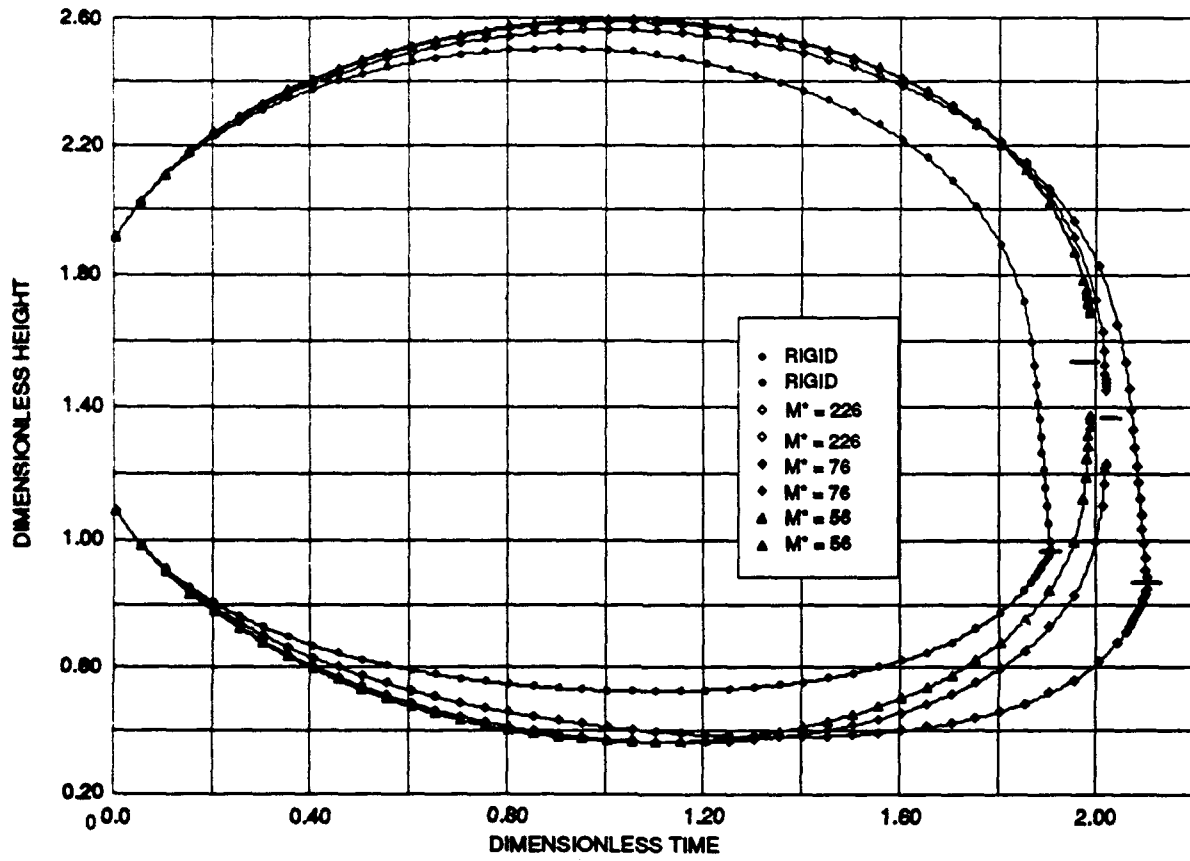


**Fig. 15.** Height of north and south poles of the bubble versus time.

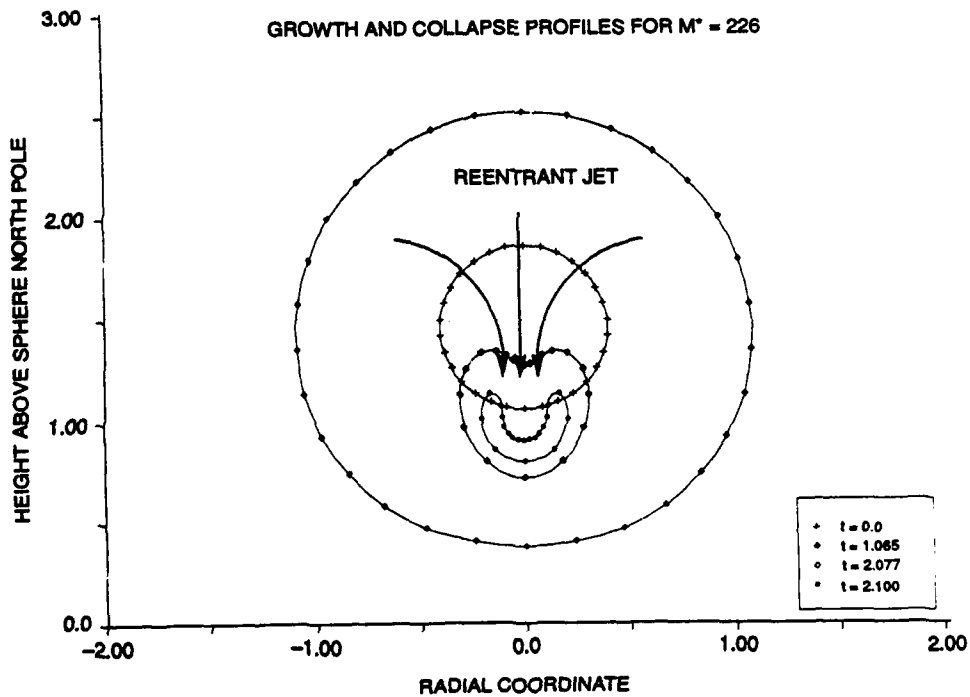
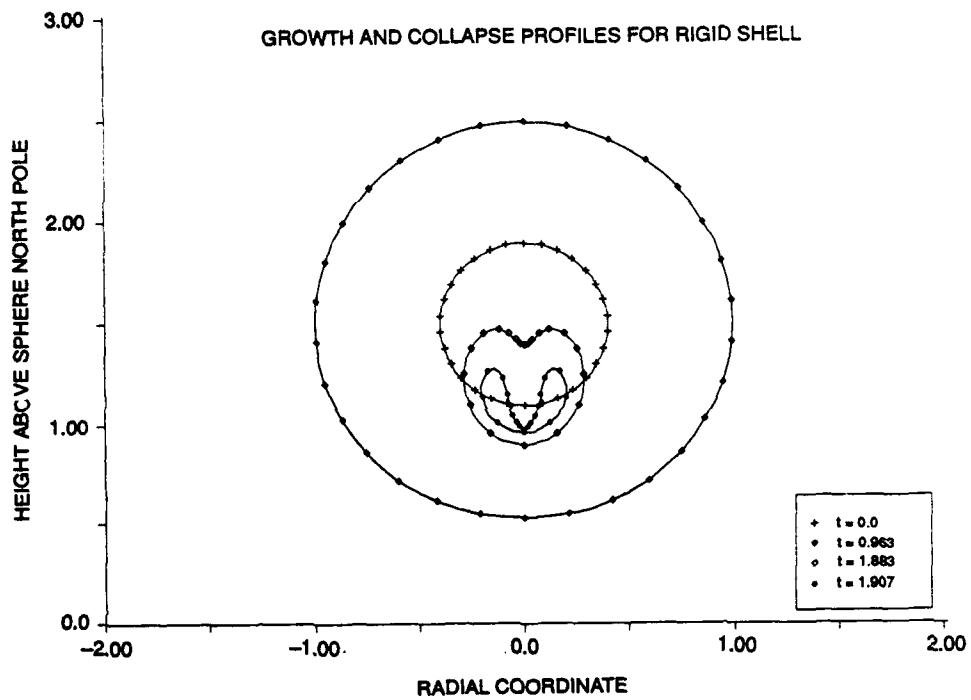


**Fig. 16.** Bubble collapse profiles at various times for collapse near rigid shell and compliant shells of  $M^* = 226, 76,$  and  $56$ .

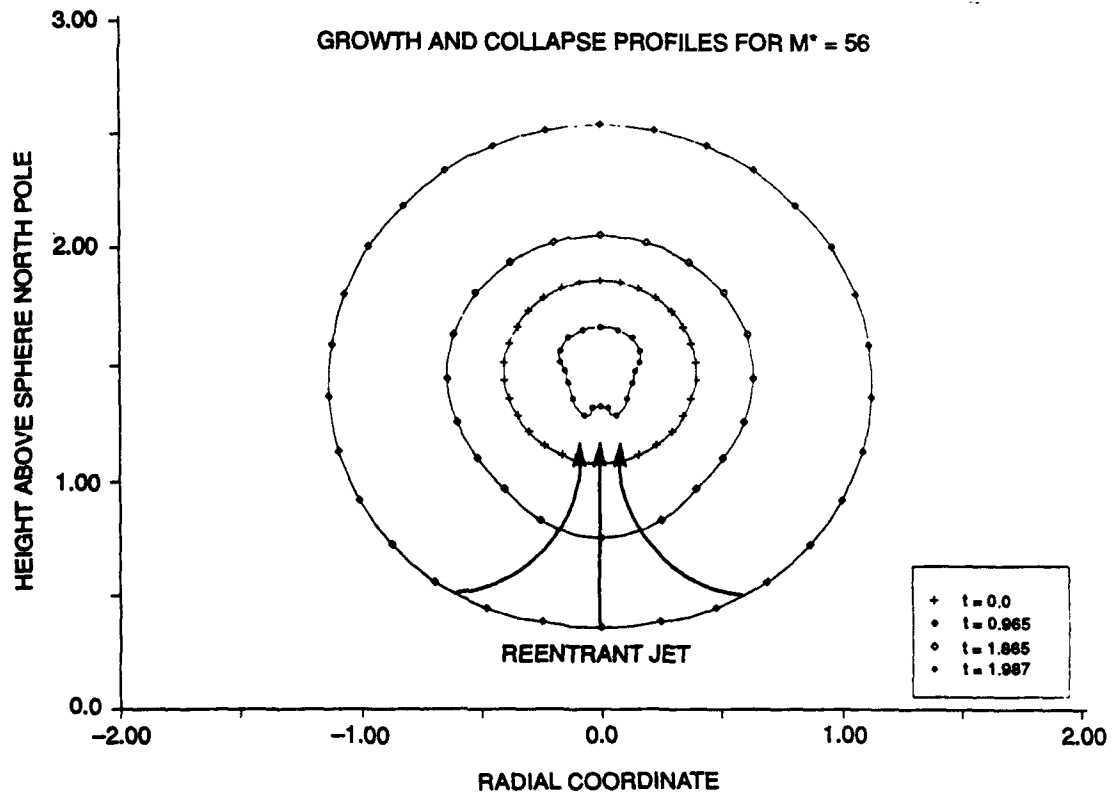
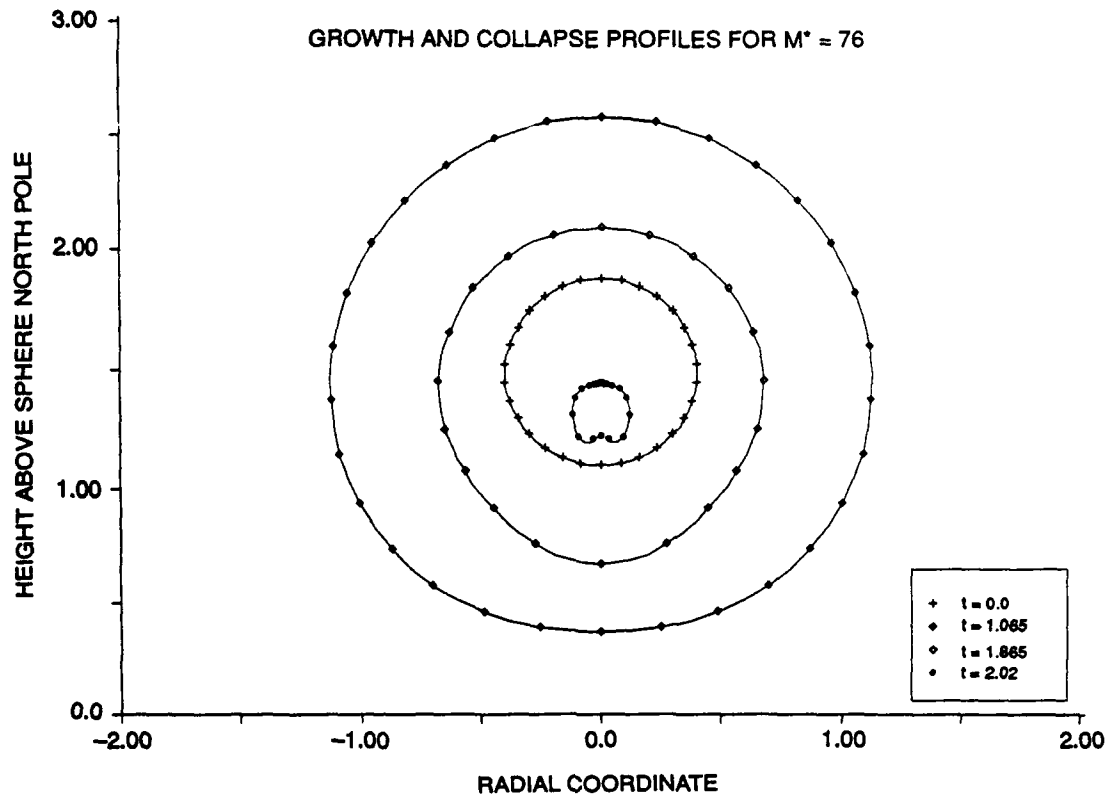


Fig. 16. (Continued)

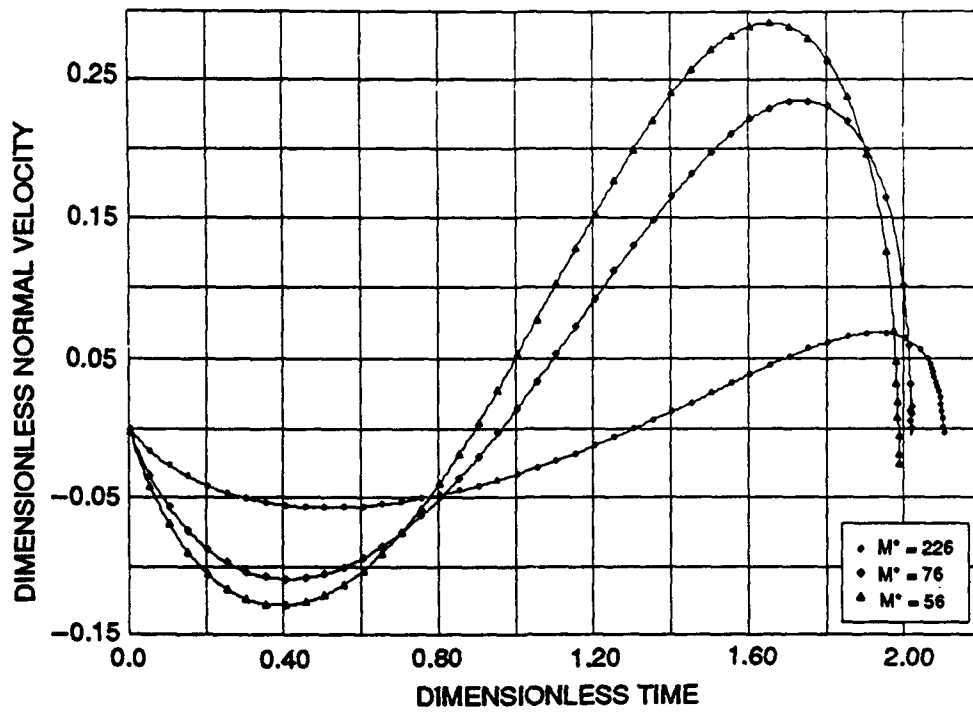


Fig. 17. Velocity (positive outward into fluid) of the north pole of the shell versus time.

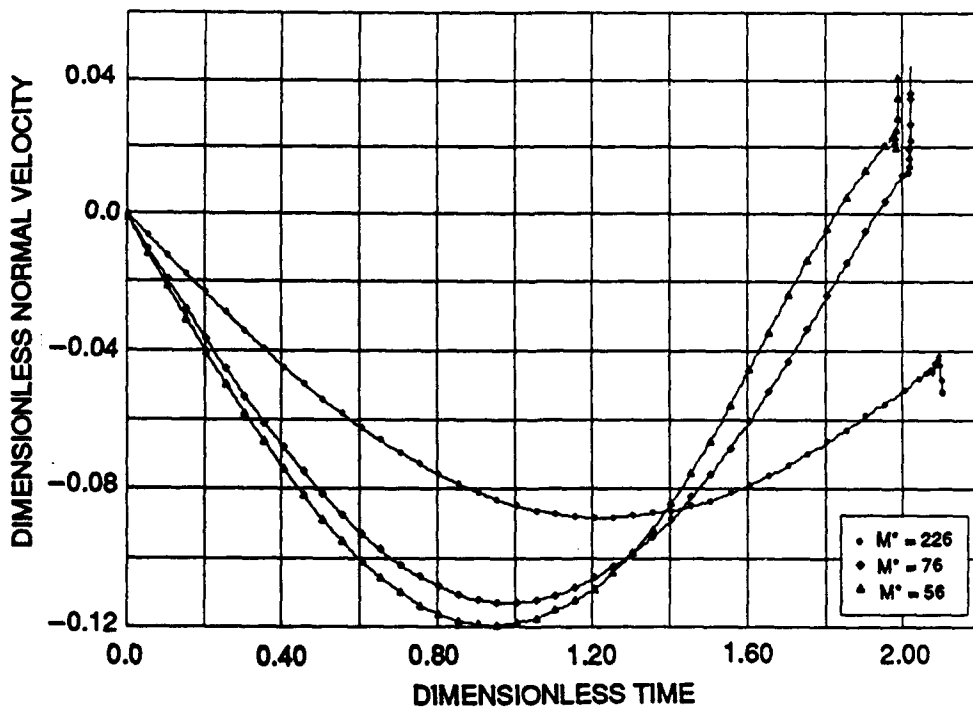


Fig. 18. Velocity (positive outward into fluid) of the south pole of the shell versus time.

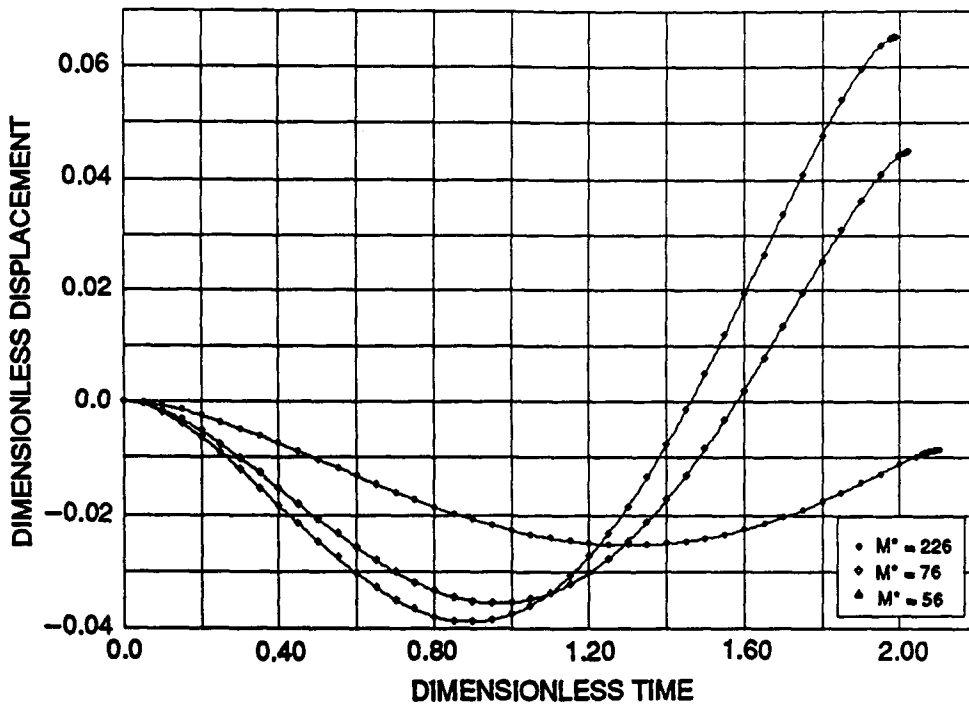


Fig. 19. Displacement of the north pole of the sphere versus time.

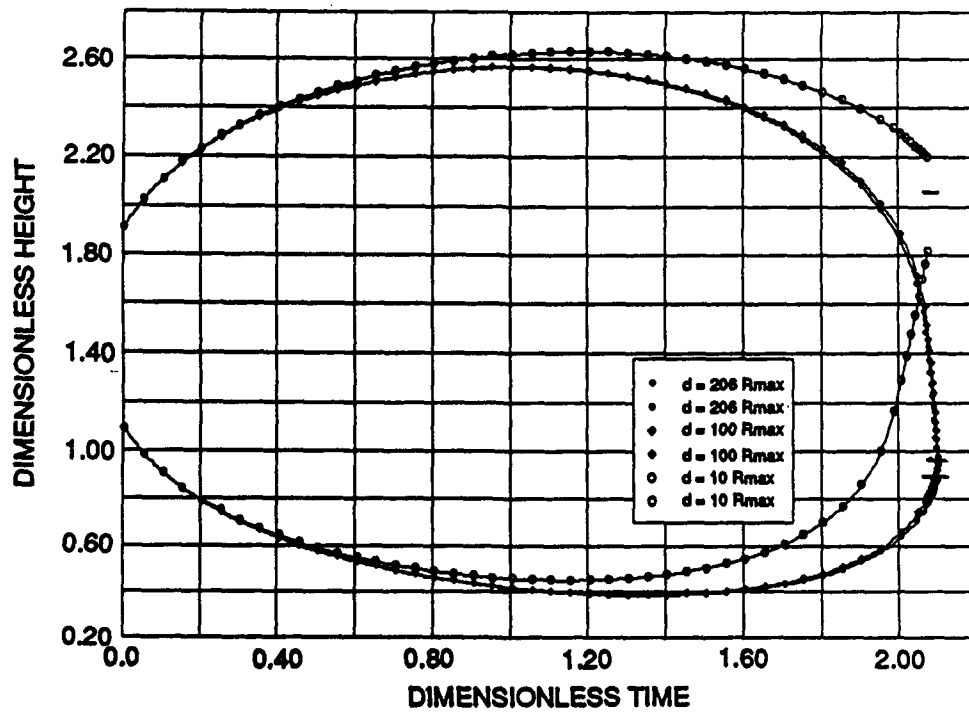


Fig. 20. Effect of gravity on the motion of the north and south poles of the bubble. Plot of height of north and south poles of the bubble versus time for shells of  $M^* = 226$ , at depths,  $d = 206 R_{max}$ ,  $100 R_{max}$ ,  $10 R_{max}$ .

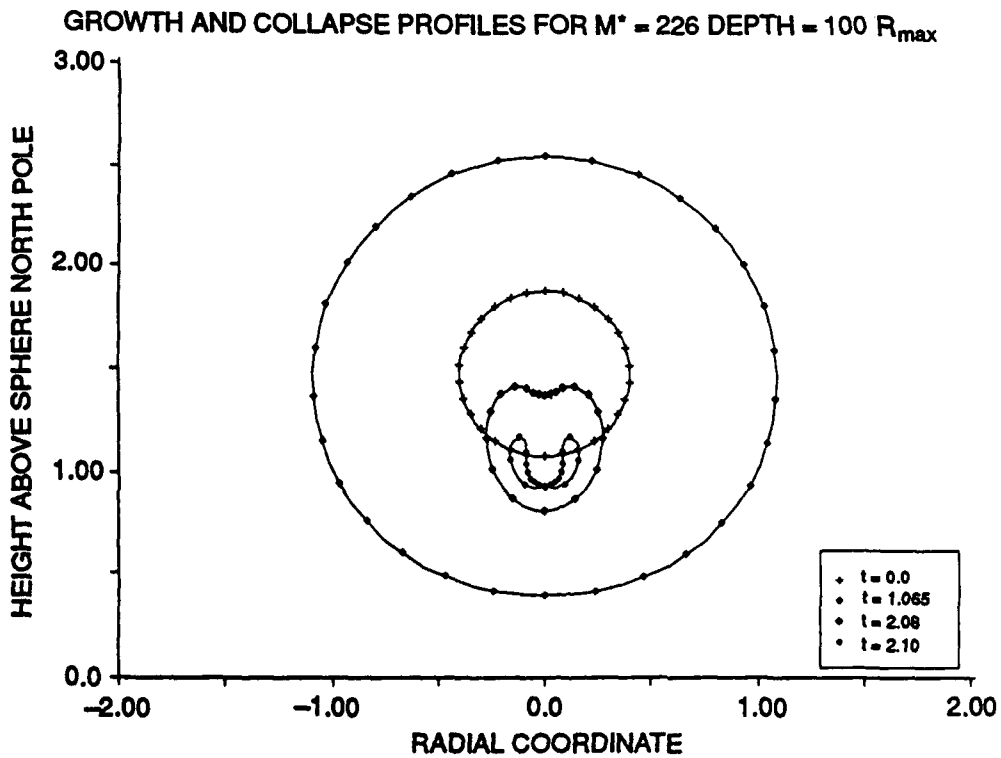
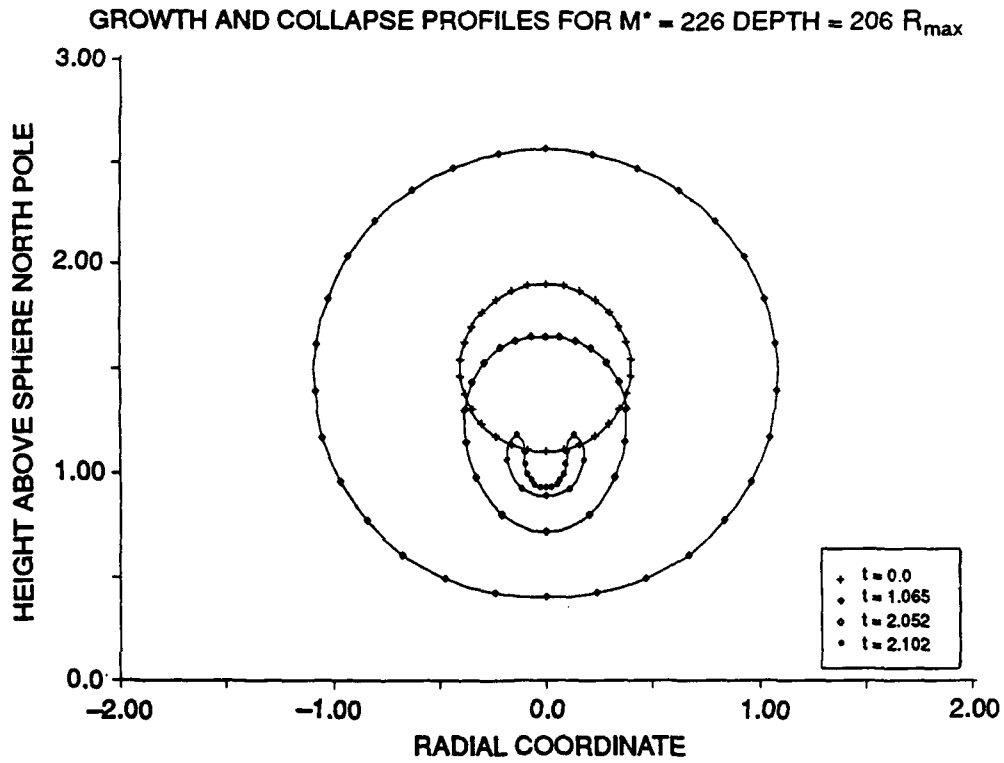


Fig. 21. Bubble collapse profiles at various times near shell of  $M^* = 226$ , at depths,  $d = 206 R_{max}$ ,  $100 R_{max}$ ,  $10 R_{max}$ .

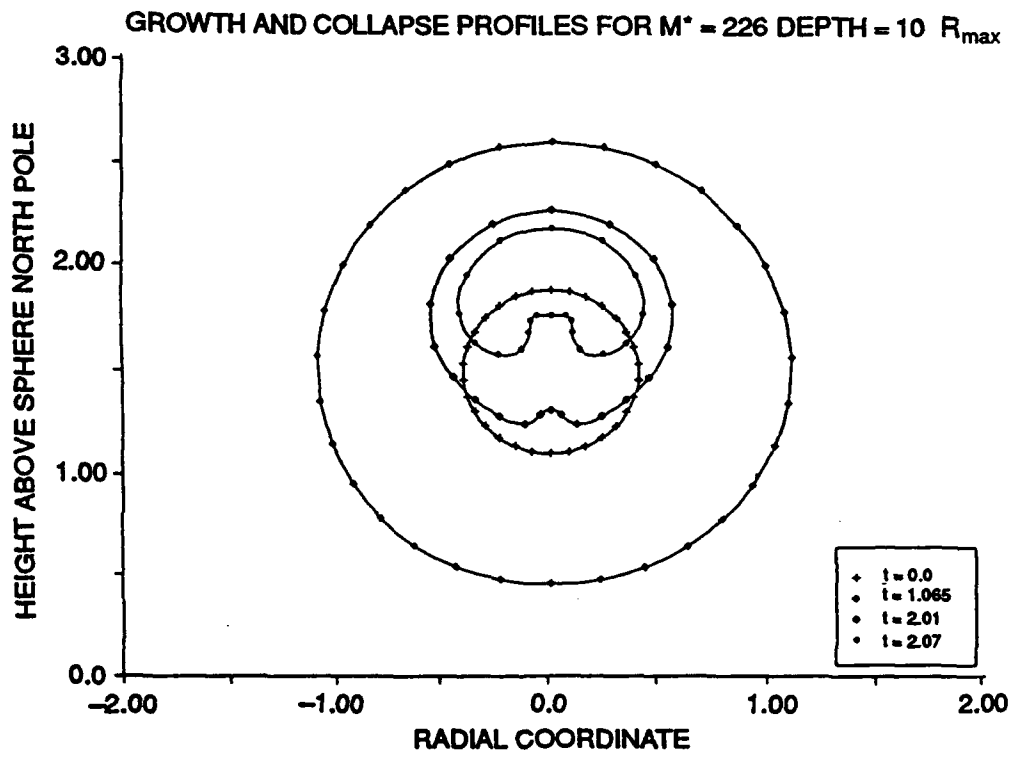


Fig. 21. (Continued)

**THIS PAGE INTENTIONALLY LEFT BLANK**

## REFERENCES

1. Roberson, J.A., and C.T. Crowe, *Engineering Fluid Mechanics*, Houghton Mifflin Company (1980).
2. Arndt, R.E., "Recent Advances in Cavitation Research," *Advances in Hydroscience*, Vol. 12 (1981).
3. Cole, R.H., *Underwater Explosions*, Dover Publications, Inc. (1948).
4. Hicks, A.N., "The Elastic Theory of Explosion Induced Whipping Motion of Ships and Submarines," Report NCRE/R532, Naval Construction Research Establishment, St. Leonards Hill Dunfermline Fife (1968).
5. Hicks, A.N., "The Theory of Explosion Induced Whipping Motions," Report NCRE/R579, Naval Construction Research Establishment, St. Leonards Hill Dunfermline Fife (1968).
6. Snay, H.G., "Underwater Explosion Phenomena: the Parameters of Migrating Bubbles," NAVORD Report 4185 (1962).
7. Benjamin, T.B., and A.T. Ellis, "The Collapse of Cavitation Bubbles and the Pressures Thereby Produced Against Solid Boundaries," *Phil Transactions*, Royal Society of London, A260 (1966).
8. Blake, J.R., and D.C. Gibson, "Cavitation Bubbles Near Boundaries," *Ann. Rev. Fluid Mech.*, Vol. 19., pp. 99-123 (1987).
9. Shima, A., Tomita, Y., Gibson, D.C., and J.R. Blake, "The Growth and Collapse of Cavitation Bubbles Near Composite Surfaces," *J. Fluid Mech.*, No. 203, pp. 199-214 (1989).
10. Duncan, J.H., and S. Zhang, "Numerical Calculations of the Growth and Collapse of a Vapor Cavity in the Vicinity of a Compliant Wall," *Mathematical Approaches in Hydrodynamics* (1990).
11. Duncan, J.H., and S. Zhang, "On the Interaction of a Collapsing Cavity and a Compliant Wall," *J. Fluid Mech.*, 226, pp. 401-423 (1991).
12. Lamb, H., *Hydrodynamics*, Dover, New York (1945).
13. Batchelor, G.K., *An Introduction to Fluid Dynamics*, Cambridge University Press, Cambridge, Massachusetts (1967).
14. Ferziger, J.H., *Numerical Methods for Engineering Application*, John Wiley and Sons, New York (1981).
15. Jaswon, M.A., and G.T. Symm, *Integral Equation Methods in Potential Theory and Elastostatics*, Academic Press, New York (1977).

### REFERENCES (Continued)

16. Anderson, D.C., *Gaussian Quadrature Formulae for  $-\int_0^1 \ln(x) f(x)dx$* , Math. Comp., Vol. 19, pp. 477-481 (1965).
17. Whang, B., "Class notes: Finite Element Methods in Engineering Mechanics," Department of Civil, Mechanical, and Environmental Engineering, George Washington University (1989).
18. Newmark, N.M., "A Method of Computation of Structural Dynamics," *Proceedings American Society for Civil Engineers*, Vol. 85, EM3 (1959).
19. Timoshenko, S., and J.N. Goodier, *Theory of Elasticity*, Maple Press Company, York, Pennsylvania (1951).
20. Hunston, D.L., Yu, C., and G.W. Bullman, "Mechanical Properties of Compliant Coating Materials," *In Laminar Turbulent Boundary Layers*, ed. E. M. Uram and H.E. Weber, ASME, New York (1984).
21. Kraus, H., *Thin Elastic Shells*, John Wiley and Sons, New York (1967).
22. Timoshenko, S., and S. Woinowsky-Krieger, *Theory of Plates and Shells*, McGraw Hill, Inc. (1959).

## INITIAL DISTRIBUTION

### Copies

#### 26 NAVSEA

1 05P, A. Malakhoff  
 1 05P1, Packard  
 1 05P2, R. McCarthy  
 1 05P2, D. Nichols  
 1 05P2, B. Martir  
 1 05P2, W. Will  
 1 05P3, Shell  
 1 05P4, Sielski  
 1 08, E. Tanner  
 1 501  
 1 5013  
 1 51  
 1 51B  
 1 5111  
 1 5112  
 1 55D  
 1 55X  
 1 55X1  
 1 55X11, D. Johansen  
 1 55X11, R. Bagbey  
 1 55X2  
 1 92R  
 1 92RP, A. Spero  
 1 PMS 350  
 1 PMS 350TB, C. Siel  
 1 PMS 08

#### 1 ONR 1132SM

R. Barsoun

#### 2 ONT

1 23, A. Faulstich  
 1 233, G. Remmers

### Copies

#### 4 OPNAV

1 21  
 1 21T  
 1 22  
 1 222

#### 4 DNA

1 (SPSD), K. Goering  
 1 (SPSD), D. Bruder  
 1 (SPSD), T. Tsai  
 1 (SSPD), M. Giltrude

#### 9 NSWC (White Oak)

1 R10A, R. Kavetsky  
 1 R10A, C. Dickinson  
 1 R102, D. Phillips  
 1 R14, J. Goertner  
 1 R14, G. Harris  
 1 R14, H. Mair  
 1 R15, R. Tussing  
 1 R15, T. Fackler  
 1 R15, R. Meriowsky

#### 12 DTIC

#### 6 SUPSHIPS/Groton, CT, Code 200

1 General Dynamics Corp.,  
 Electric Boat Div. /Via SUPSHIP  
 1 Code 442, G. Leon  
 1 Code 443, D. Church  
 1 Code 447, G. Peteros  
 1 Code 457, C. Fast  
 1 Code 457, A. Wagner

**INITIAL DISTRIBUTION (Continued)**

|               |                              |               |               |             |                 |
|---------------|------------------------------|---------------|---------------|-------------|-----------------|
| Copies        |                              |               | 1             | 1740.3      | B. Rhee         |
| 3             | SUPSHIPS/Newport News, VA    |               | 1             | 1740.3      | L. Ripley       |
| 1             | Newport News Shipbuilding    |               | 1             | 175         | J. Sykes        |
|               | Via SUPSHIP                  |               | 1             | 1750.1      | B. Whang        |
|               |                              |               | 1             | 1750.1      | D. Bond         |
| 1             | Code E12, D. Alexander       |               | 1             | 1750.1      | W. Gilbert      |
| 1             | Code E12, T. Heldreth        |               | 1             | 1750.1      | W. Gottwald     |
| 1             | USNA                         |               | 10            | 1750.1      | C. Milligan     |
|               | Technical Library            |               | 1             | 1750.1      | C. Nguyen       |
|               |                              |               | 1             | 1750.1      | F. Rasmussen    |
|               |                              |               | 1             | 1750.1      | B. Rose         |
| 1             | Sandia National Laboratories |               | 1             | 1750.1      | T.P. Schweich   |
|               | L. Weingarten                |               | 4             | 1750.1      | S. Zilliacus    |
|               |                              |               | 1             | 1750.2      | W. Conley       |
|               |                              |               | 1             | 1750.2      | D. Hagar        |
|               |                              |               | 1             | 1750.2      | M. Hoffman      |
|               |                              |               | 1             | 1750.2      | B.A. Tegeler    |
|               |                              |               | 1             | 1750.2      | G. Waldo        |
|               |                              |               | 1             | 177         | R. Fuss         |
|               |                              |               | 1             | 1770.1      | M. Riley        |
|               |                              |               | 1             | 1770.1      | F. Costanzo     |
|               |                              |               | 1             | 19          | M. Sevik        |
| <b>Copies</b> | <b>Code</b>                  | <b>Name</b>   | <b>Copies</b> | <b>Code</b> | <b>Name</b>     |
| 1             | 0012                         | B. Douglas    | 1             | 341         | Publications    |
| 1             | 0014                         | L. Becker     | 1             | 3421        | TIC (C)         |
| 1             | 1280                         | G. Everstine  | 10            | 3432        | Reports Control |
| 1             | 1282                         | E. Brooks     |               |             |                 |
| 1             | 1282                         | R. Lipman     |               |             |                 |
| 1             | 15                           | W. Morgan     |               |             |                 |
| 1             | 17                           | M. Krenzke    |               |             |                 |
| 1             | 1702                         | J. Corrado    |               |             |                 |
| 1             | 172                          | R. Rockwell   |               |             |                 |
| 1             | 1720.3                       | K. Nishida    |               |             |                 |
| 1             | 1720.4                       | N. Gifford    |               |             |                 |
| 1             | 1720.4                       | E. Rasmussen  |               |             |                 |
| 1             | 1720.4                       | A. Wiggs      |               |             |                 |
| 1             | 173                          | J. Beach      |               |             |                 |
| 1             | 174                          | I. Hansen     |               |             |                 |
| 1             | 1740.1                       | T. Burton     |               |             |                 |
| 1             | 1740.2                       | F. Fisch      |               |             |                 |
| 1             | 1740.2                       | D. Wilson     |               |             |                 |
| 1             | 1740.3                       | H. Gray       |               |             |                 |
| 1             | 1740.3                       | D. Kornhauser |               |             |                 |
| 1             | 1740.3                       | S. Poy        |               |             |                 |